Science Advances
AAAS

Supplementary Materials for

Tropical mountain ice core $\delta^{18}O$: A Goldilocks indicator for global temperature change

Zhengyu Liu *et al.*

Corresponding author: Zhengyu Liu, liu.7022@osu.edu

Sci. Adv. **9**, eadi6725 (2023)
DOI: 10.1126/sciadv.adi6725

This PDF file includes:

Texts S1 to S6
Figs. S1 to S19
References

Supplementary Text

Text 1: Deglaciation evolution over Sajama

The deglacial evolution of $\delta^{18}O_{ice}$ can also be compared with iTRACE on another Andean ice core, Sajama (*5*), as shown in Fig. S3. Again, the model topography at Sajama (2631-m) is much lower than the ice core (6540-m) in iTRACE. Similar to the comparison over Huascarán (Fig. 1a-d), $\delta^{18}O_p$ and $\delta^{18}O_v$ in the lower atmosphere in iTRACE are dominated by millennial variability reflecting the amount effect (Fig. S3c, d), but in the middle and upper troposphere this changes and is dominated by an enrichment trend (Fig. S3a, b), reflecting the temperature effect associated with deglacial warming. Meanwhile, the Sajama $\delta^{18}O_{ice}$ record exhibits much stronger millennial variability than Huascarán $\delta^{18}O_{ice}$ and model $\delta^{18}O_p$ and $\delta^{18}O_v$ over the Andes, and in the tropics in general. This $\delta^{18}O_{ice}$ behavior in Sajama is more complex than that in Huascarán and is somewhat different from those in the tropics overall. This can be caused, we hypothesize, by several reasons. First, Sajama is located on the margin of tropics and, furthermore, over the Altiplano Plateau in a very dry environment, such that the $\delta^{18}O_{ice}$ may be affected substantially by the sublimation process (*88*, *89*). Second, Huascarán can be treated simply like a "weather station tower" that passively records the mid-troposphere temperature, because it is on an isolated mountain peak in the deep tropics with little perturbation on the atmospheric circulation. In contrast, Sajama is located over the Altiplano Plateau, which could exert a strong perturbation on the mid-level atmospheric circulation, such that the Sajama record may contain significant regional response signal of the atmospheric circulation and remote moisture changes, as studied previously for the central Andes (*29–34*).

Text 2: $\boldsymbol{\delta^{18}O}$ variability over Andes and the tropics

Deglacial climate-isotope variability over the tropical Andes is representative of the tropics. This can be seen in the largely zonally uniform correlation $cor < \delta^{18}O_v, T >$ over the globe at different levels (Fig. S4). The correlation in the tropics changes from negative (amount effect) on the surface ($\sigma = 1$) and lower atmosphere ($\sigma = 0.81$, about 800 hPa or 3000-m) to positive in the mid-troposphere ($\sigma = 0.5$, about 500 hPa or 6000-m) and upper-troposphere ($\sigma = 0.3$, about 300 hPa or 8000-m) over the entire tropics, except over Tibetan-Iran Plateau in the mid-atmosphere.

The similarity between the $\delta^{18}O_v$ variability over the Andes and that over the entire tropics is consistent with the moisture sources mainly from the tropics in the atmospheric column over Andes (*22*), which is further confirmed by our moisture tracking tagging experiments. Two water tagging experiments are analyzed here for the LGM (20ka) and PI in the atmospheric component model of iCESM1.3 (iCAM5.3) of nominal 2^o resolutions. Each experiment is integrated for 40 years with the last 20 years of data analyzed. For each experiment, the model is forced by the climatology of monthly SST, sea ice distribution and sea surface $\delta^{18}O$ and δD extracted from the iTRACE experiment, as well as the continental ice sheet, orbital parameters and GHG concentrations just as in iTRACE. We tagged 25 regions over the globe, including 13 regions in the ocean and 12 over the land (*18*). The source contribution to moisture (dash) and heavy isotope (solid) at each pressure level are shown for the Andean region (Fig. S5a) and the entire tropics (Fig. S5b) at PI, with the distribution to isotope value shown in Fig. S5c and S5d, respectively. In the mid- to upper- troposphere, the dominant contribution of both moisture ($^{16}O_v$) and $\delta^{18}O_v$ are from the tropical Atlantic Ocean for Andes (Fig. S5a, c) and are from tropical ocean for the tropics overall (Fig. S5b, d). The contributions are similar at LGM (not shown).

Text 3: Surface isotope response

Near surface isotope response during deglaciation is determined by two factors, the dynamic response associated with the amount effect and the sea water $\delta^{18}O_{sw}$ effect from the meltwater. Globally, the negative $cor < \delta^{18}O_v, T >$ in the tropical lower atmosphere (Fig. S4c, d) appears similar to that for precipitation $cor < \delta^{18}O_p, T >$ (Fig. S9b). This negative $cor < \delta^{18}O_p, T >$ appears consistent with the negative correlation between $\delta^{18}O_p$ and local precipitation amount in the tropics (Fig. S9c) as in the amount effect. Physically, the deglacial surface warming in the tropics leads to increased precipitation (Fig. S9d) and, in turn, negative $\delta^{18}O_p$ and lower atmosphere $\delta^{18}O_v$ due to the amount effect. This is confirmed in the analysis of the responses to individual forcing of greenhouse gases, orbital forcing and ice sheet, which also show regions of negative $cor < \delta^{18}O_p, T >$ in the equatorial region (not shown). This negative relationship between isotopes and temperature has been observed often in tropical Andes regions because high temperatures and rainy season tend to coincide (*90*). However, this negative $cor < \delta^{18}O_p, T >$ is also contributed by the change of sea water $\delta^{18}O_{sw}$ during the deglaciation, as analyzed in the response to meltwater forcing alone in iTRACE. During deglacial warming, meltwater injects highly negative isotope $\delta^{18}O$ from the continental ice sheet of -30 to -40‰ into the ocean, leading to the depletion of $\delta^{18}O_{sw}$ of a magnitude of 1‰ during the entire deglaciation associated with the 100-m sea level rise (*42*). As the ultimate source, this depleted sea water $\delta^{18}O_{sw}$ directly decrease the $\delta^{18}O_v$ in the lower atmosphere and $\delta^{18}O_p$ in the tropics with a comparable magnitude (not shown). Furthermore, this melting water induced depletion is of the same sign as the warming induced depletion due to the amount effect, reinforcing each other. The combined effects of climate forcing and $\delta^{18}O_{sw}$ leads to the wide-spread negative region of negative $cor < \delta^{18}O_p, T >$ in the tropics in iTRACE (Fig.S9b). It should be noted, however, that, in spite of its large impact on the $\delta^{18}O_v$ in the lower atmosphere, $\delta^{18}O_{sw}$ does not exert a major impact on the $\delta^{18}O_v$ response in the middle and upper troposphere, because the change of $\delta^{18}O_v$ in the upper troposphere has a much greater amplitude than 1‰, as seen, for example, over Huascarán in model and observations (Fig. 1a and b).

Text 4: δD_v response to ENSO

The vertical structure of δD_v can be first inferred from its interannual variability in response to ENSO through the correlation between the Nino 3 index and monthly δD_v at different heights. In TES, the δD_v response to ENSO changes its sign with height in the tropics, regionally, from the surface (as in the amount effect) to middle and upper troposphere (as in the temperature effect) in the tropics, notably in the central and western equatorial Pacific (Fig. S10a). This is consistent with a previous analysis of Sutanto et al. (*46*), in which they only analyzed two levels (1000 hPa and 500 hPa). A similar sign change of correlation with ENSO is also seen in the iTRACE model (Fig. S10b) and HighRes model (not shown). This sign change is also consistent with the correlation of IASI δD_v, which is available only above 700 hPa (Fig. S10c). It is also worth noting that the response pattern to ENSO in IASI is more similar to iTRACE than TES, implying some discrepancies/uncertainties between the two satellite measurements. Since the atmospheric temperature response tends to be of the same sign in the troposphere column, this sign change of ENSO response is consistent with a change of the sign of δD_v variability as shown in Fig. 3. It should also be noted that the $\delta^{18}O_v$ sign reversal is locally relative to the surface, which is consistent with our RCE theory (Method 4), suggesting that the reversal is caused by local convection.

Text 5: Temporal slope $\Delta\delta^{18}O_v/\Delta T$

Over Huascarán, the range of deglacial change of $\delta^{18}O_v$ and temperature are about 7‰ and 7ºC in the model (Fig. S7a, b), corresponding a temporal slope of $\Delta\delta^{18}O_v/\Delta T \approx 1‰/\ ^{o}C$ (Fig. S7c, d), as seen in the difference between LGM and PI over the Andes. This temporal slope value appears close to the spatial slope derived from present surface observations over Antarctica (*10*), but this is, we believe, an accident. Indeed, the Antarctic spatial slope near the surface is reduced by about 30% from that in the free atmosphere due to the strong inversion layer there. In the free atmosphere, the spatial slope over Antarctica should be greater than the temporal slope in general as shown in the Unified Slope Equations (*76*).

In the tropics, temperature and isotopes vary predominantly in the vertical direction. This vertical spatial slope with elevation for δD_v can be inferred from the scatter plot of δD_v versus temperature at different pressure levels for the satellite measurements of TES and ISAI. Both spatial slopes are about $7‰/\ ^{o}C$ (Fig. S15a). This is consistent with the spatial slope of iTRACE at PI, and LGM (Fig. S15a), suggesting the model reproduces the spatial slope in agreement with current observations, and the spatial slope does not change substantially at LGM.

For $\delta^{18}O_v$, the vertical spatial slopes can also be calculated similarly from the scatter diagram of $\delta^{18}O_v$ and temperature in iTRACE PI and LGM while the deglacial temporal slope at a specific level can be seen as the line connecting LGM and PI of the same level (neglecting the 120-m sea level change) (Fig. S15b). The spatial and temporal slopes appear to change substantially in the free atmosphere below and above 450 hPa. From 700 hPa to 450 hPa (including the level of Huascarán), the spatial slopes are $0.84‰/\ ^{o}C$ and $1.34‰/\ ^{o}C$ for PI and LGM respectively, while the deglacial temporal slope averaged over these levels is $0.46‰/\ ^{o}C$; from 450 hPa to 100 hPa, the spatial slopes for PI and LGM are $1.27‰/\ ^{o}C$ and $1.36‰/\ ^{o}C$, while the deglacial temporal slope averaged over these levels is $1.06‰/\ ^{o}C$. Therefore, across all levels in the free atmosphere, the temporal slope is always smaller than the spatial slope. This is consistent with the United Slope Equations derived from the Rayleigh theory (*76*) and our model tropical process is close to Rayleigh (Fig. S14). Furthermore, all the slopes increases with height, which can be understood as resulting from the colder temperature with elevation and in turn an increased saturation moisture lapse rate following the Clausius–Clapeyron relationship (*76*, *91*). This increased temporal slope towards the upper troposphere has been seen in the tropics in their spatial plot (Fig. 2b, S6c, d, S7c, d). Relatively to the lower atmosphere, nevertheless, spatial slopes are close to the temporal slope above 450 hPa and remain almost with elevation. This feature, we speculate, is caused by the strong mixing and entrainment/detrainment there.

Text 6: Huascarán temperature as a Goldilocks indicator for global mean temperature change

Qualitatively, our iTRACE simulation demonstrates that the deglacial temperature change at Huascarán is a good indicator of the temperature change not only in the tropical middle and upper troposphere, but also in other atmospheric levels in the tropics and for the global mean. This is evident in the similar temporal evolution pattern of temperature in different levels in the tropics (dash) and the globe (solid) (Fig. S17a). The similarity becomes even clearer in the evolution of these temperatures normalized by their respective magnitude (standard deviation) (Fig. S17b). The similarity of the (normalized) tropical temperature evolution at different levels reflects the control of the surface temperature on the tropospheric column through deep convection, while the increased magnitude with height is caused by the response of the moisture atmospheric lapse rate to GHGs forcing (*61*). The similarity of tropical temperature to GMST, on the other hand, reflects the proximity of the tropics to the node point of the interhemispheric bipolar see-saw of temperature accompanying the changing Atlantic Meridional Overturning Circulation (AMOC). This is more evident in Fig. S17c and d for the absolute and normalized surface temperature changes in different latitude bands in comparison with GMST. It has been shown that the weakening of AMOC in HS1 and YD causes a bipolar see-saw response with strong cooling and warming in the Northern and Southern Hemisphere, respectively, but only a small impact in the tropics. This bipolar see-saw temperature response is almost canceled in the global mean, leaving muted millennial variability superimposed on a strong deglacial warming trend in GMST, similar to the tropics. As a result, the temperature evolution in the tropical atmospheric column is highly correlated with GMST (Fig. S17e). This muted HS1 and YD events superimposed on the deglacial warming trend in iTRACE is consistent with the reconstructions of global mean air temperature (*59*) and SST (*59*, *62*) (blue curve in Fig. 4b and c).

Furthermore, climate models show that the deglacial temperature change in the Huascarán ice core could also serve as a quantitative indicator of the GMST change. We first examine this in iTRACE. Indeed, the deglaciation temperature evolution in Fig. S17a already shows that the tropical temperature change near the level of Huascarán (near 500 hPa, red dash) is of comparable magnitude with that of the GMST evolution (black solid), while the tropical temperature change above Huascarán (300 hPa, yellow dash) and below Huascarán (800 and 1000 hPa, blue and black dash) has a magnitude greater and smaller than the GMST change, respectively. More clearly, Fig. 4a shows that the deglacial temperature changes are almost identical between the Huascarán site and GMST. Fig. 4d shows the global distribution of the zonal-mean deviation (root-mean-square-error) of the deglacial temperature evolution from GMST. The minimum deviation is confined in the tropical mid-troposphere temperature around the latitude of Huascarán. This is consistent with the temporal evolution of Huascarán temperature that almost parallels that of GMST in both the pattern and magnitude (Fig. 4a). This feature of nearly equal temperature change of Huascarán and GMST is a result of two characteristics of the deglacial global temperature response, which can be illustrated from the LGM-PI difference. First, the magnitude of temperature change is almost the same in the tropics and global mean at the mid-troposphere level (around 450 hPa). This is evident in the vertical profiles of the iTRACE temperature responses of the tropical mean and global mean, which intersect at about 450 hPa (Fig. S18a, red dot and solid). Second, in the lower atmosphere (below 450 hPa to the surface), the magnitude of global mean temperature response decreases very little, in contrast to the clear decrease of the tropical mean temperature response (Fig. S18a, red solid and dot). These two response characteristics can be understood from the different vertical profiles of the deglacial temperature responses between low and high latitudes. As seen in the global zonal mean response, the LGM-PI cooling intensifies upward in low latitudes from -4ºC near the surface to -9ºC at 200 hPa (contours in Fig. S6a, also Fig. S17a), but intensifies downward at high latitudes from almost 0ºC at 200 hPa to about 10ºC at the surface (Fig. S6a), leading to the well-known polar amplification near the surface, but a "tropical amplification" in the upper troposphere. The upward increase of temperature response with height in the tropics is a robust feature of the climate response to GHGs forcing due to the change of moist atmospheric lapse rate (*61*). In high latitudes, the downward increase of temperature response towards the surface, and the resulting polar amplification near surface, are caused by positive temperature feedbacks in high latitudes, notably the surface albedo feedback and the dynamic amplifier that is caused by the poleward atmospheric heat transport (*92*). In particular, in the glacial period, this positive feedback and, in turn, the polar surface cooling is amplified strongly by the expansion of sea ice coverage and the associated albedo feedback. The opposite responses of vertical temperature profiles between the low and high latitudes lead to a level of almost uniform cooling (about -6 to -7ºC) in the mid-troposphere around 450 hPa. Furthermore, below this level towards the surface, the strong downward increase of the temperature response at high latitudes tends to offset the downward decrease of temperature response at low latitudes, leaving little vertical change in the global mean temperature in the lower atmosphere. Thus, the temperature change in the tropical mid-troposphere, albeit greater than the surface temperature change locally in the tropics, tends to be comparable with the GMST change.

The temperature responses discussed for iTRACE above are robust in the HighRes model as well as in models of Paleoclimate Model Intercomparison Project (PMIP3 models:CCSM4, GISS-E2-R, MRI-CGCM3, MIROC_ESM; PMIP4 models: AWI-ESM, MIROC-ES2L, MPI-ESM; an outlier IPSL-CMSR-LR is not include) (*64*). In the vertical profiles of the LGM-PI temperature difference, the magnitude of tropical cooling equals approximately that of the global mean cooling at the level of around 450 hPa while the cooling magnitude does not change substantially in the lower atmosphere for the global mean, as seen in individual models (Fig. S18a) and their ensemble mean (Fig. S18b). As a result, the deviation (absolute value) between the temperature response at each grid point in the atmospheric column and the GMST response tends to exhibit a minimum region in the tropical mid-troposphere in most PMIP models, and in the ensemble mean (Fig. S19).

We note that due to the change of ice sheet topography during deglaciation, the comparison of near surface temperature changes at different times outside the tropics should remove the elevation effect (*93*). There are several approaches to "remove" this elevation effect, which, nevertheless, has little impact on the GMST response. The first approach is to extrapolate the temperature to below the topography to 1000 hPa using a lapse rate 7.6ºC/100hPa (*93*) as the "virtual" temperature, as if there were no topography (No-Topo), and the global mean temperature calculation will include these "virtual" temperatures. This No-Topo approach is used in Fig. 4, S17, S18a, b and S19. The second approach is to use the LGM topography (LGM-Topo). Now, the global mean air temperatures at different times are all calculated only for those grid points above the LGM topography. This is done in Fig. S18c and d. In comparison with the approach of No-Topo in Fig. S18a and b, this temperature change exhibits a slightly weaker cooling near the surface in the global mean, because it does not take into account the stronger cooling below ice sheets, mainly in Antarctica. A third approach is to use the realistic topography at each time (Real-

Topo), in which the global mean temperature at each level is calculated for those grid points above the realistic topography at that time. The deglacial global mean temperature change thus produced is also very close to the other two approaches (not shown).

Supplementary Figures

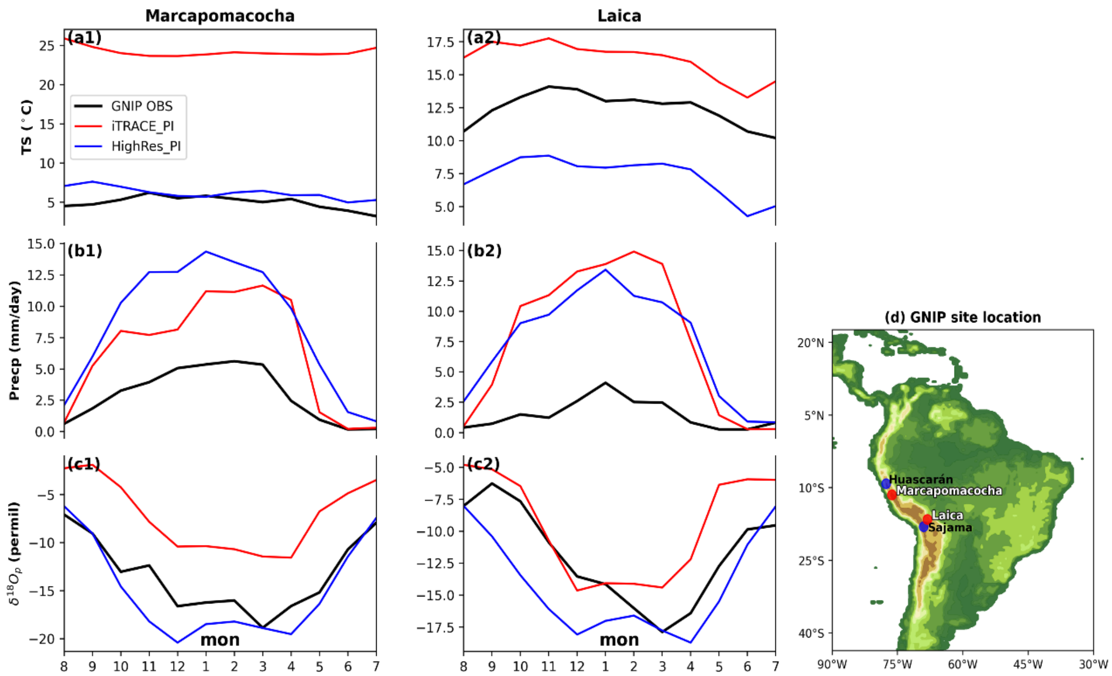

Fig. S1: Model-data comparison over Andes. Seasonal cycle of surface temperature (top row: °C), precipitation (mid row: mm/day) and δ^{18}Op (bottom row: permil) at two GNIP stations in the Andean region (black) in comparison with the preindustrial (PI) climatology of iTRACE (red) and HighRes (blue): (a1-c1): Marcapomacocha (76.3°W, 11.4°S), the elevation is 4400m at the real site, but 1128m and 4545m in iTRACE and HighRes models, respectively; (a2-c2): Laica (68.1°W, 16.5°S), the elevation is 3940m at the real site, but 2250m and 3863m in iTRACE and HighRes models, respectively.

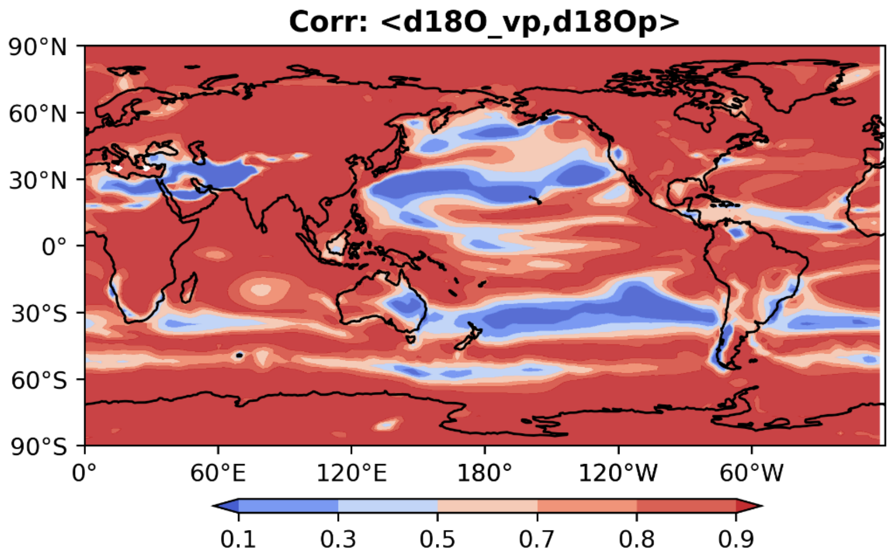

Fig. S2: Global map of the correlation between surface $\delta^{18}O_{vp}$ and $\delta^{18}O_p$ during the last deglaciation in iTRACE: Correlation between the surface vapor $\delta^{18}O_v$ weighted by precipitation $\delta^{18}O_{vp}$ and the precipitation $\delta^{18}O_p$ at each grid point. All correlations are made between 20 and 11ka after creating 500-year running means. The correlation is similar for $\delta^{18}O_v$ without the weighting of precipitation.

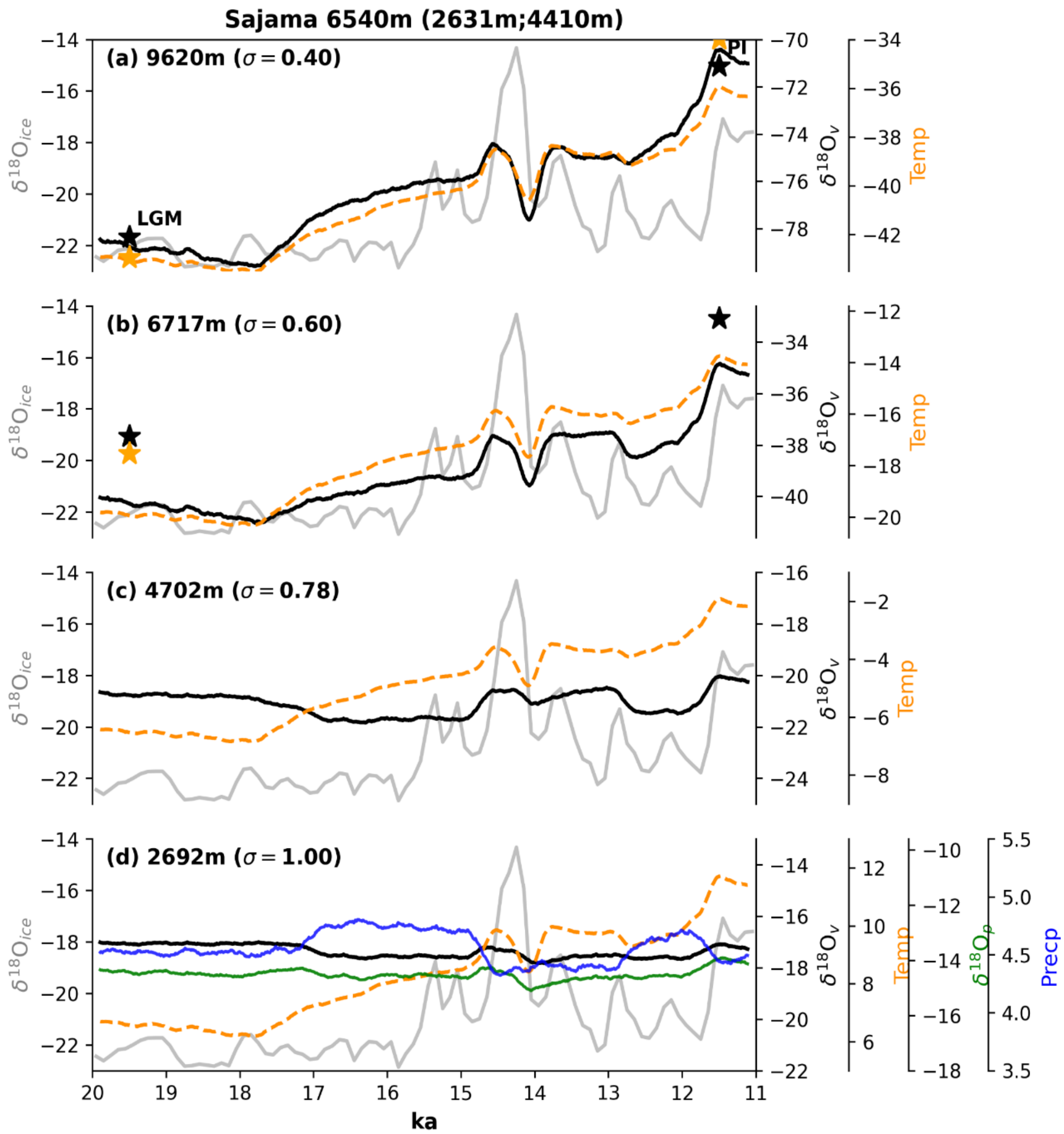

Fig. S3: Model-data comparison for the last deglaciation on Sajama. Time series of ice core $\delta^{18}O_{ice}$ (grey, in permil) in the Sajama compared with the iTRACE model (200-year running mean) vapor $\delta^{18}O_v$ (black, in permil) and temperature (orange, in °C) at different altitudes (sigma-levels), and, additionally, precipitation (blue, in mm/day) and precipitation $\delta^{18}O_p$ (green, in permil) at the surface (d). Also shown in (a,b) are the $\delta^{18}O_v$ (black star) and temperature (orange star) in the HighRes iCAM model at LGM and PI, marked at 19.5ka and 11.5ka, respectively, with the $\delta^{18}O_v$ offset by 9 and 4 permil in a) and b), respectively.

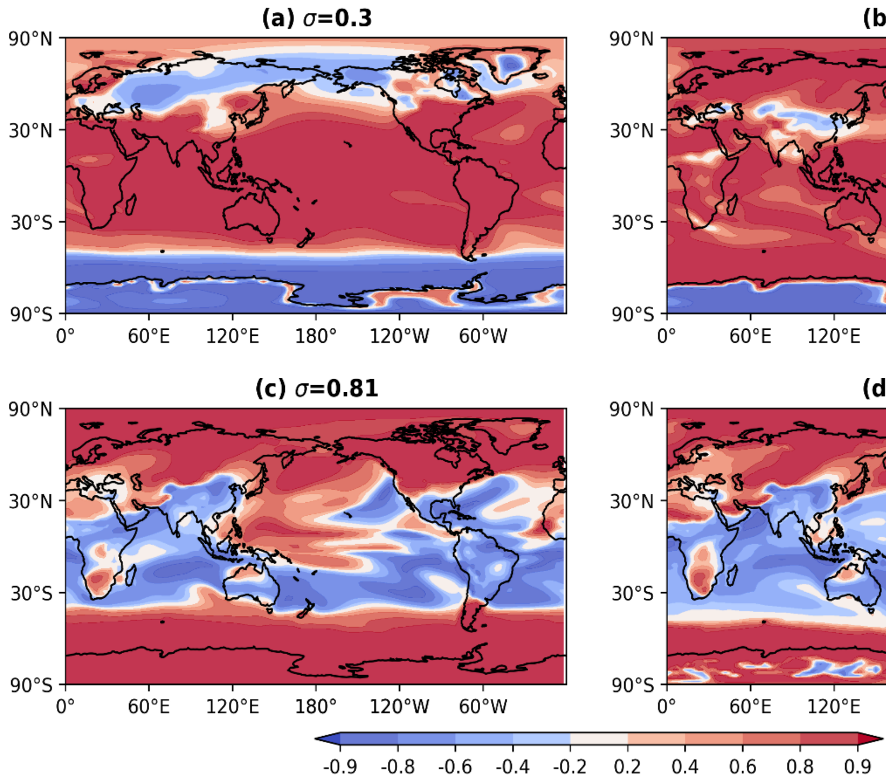

Fig. S4: Correlation maps between $\delta^{18}O_v$ and temperature cor $< \delta^{18}O_v, T >$ on different levels during the last deglaciation in iTRACE. (a) Upper troposphere level $\sigma = 0.3$; (b) mid-troposphere level $\sigma = 0.5$; (c) lower troposphere level $\sigma = 0.81$; (d) surface level $\sigma = 1.0$. The correlation is taken at the same grid point. Here, σ is the sigma level such that $\sigma = 1$ at surface and $\sigma = 0$ at the top atmosphere. The altitude of the σ level changes with bottom topography and corresponds to approximately the pressure levels of 300, 500, 800 and 1000 hPa for $\sigma = 0.3, 0.5, 0.8$ *and* 1, respectively, over the global ocean. The correlation in the tropics changes from negative (amount effect) on the surface to positive in the mid-atmosphere except over Tibetan-Iran Plateau. All correlations are calculated for 20-11ka after creating 500-year running means.

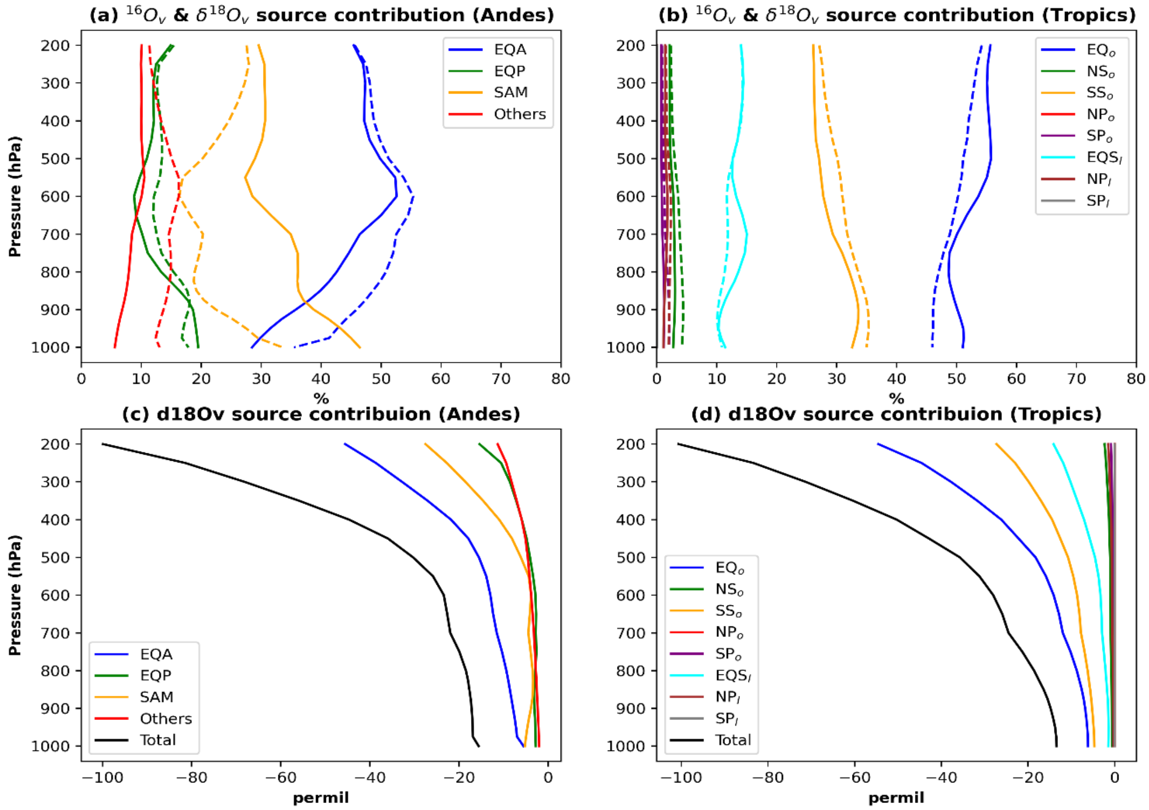

Fig. S5: Contribution of moisture (O_v^{16}) and $\delta^{18}O_v$ from different source regions to the Andes and tropical region. Percentage contribution of O_v^{16} (solid lines) and $\delta^{18}O_v$ (dashed lines) from different source regions at each pressure level over (a) the Andes and (b) the tropics (20ºS-20ºN). Absolute contribution of $\delta^{18}O_v$ from each source region to the (c) Andes and (d) tropical region. For the Andean region, the tagged source regions are divided into tropical Atlantic Ocean (EQA), tropical Pacific Ocean (EQP), South America continent (SAM), and other regions. For the tropics, the tagged source regions are divided into tropical ocean (EQ_O), northern subtropical ocean (NS_O), southern subtropical ocean (SS_O), northern polar ocean (NP_O), southern polar ocean (SP_O), tropical and subtropical land (EQS_l), northern polar land (NP_l), and southern polar land (SP_l).

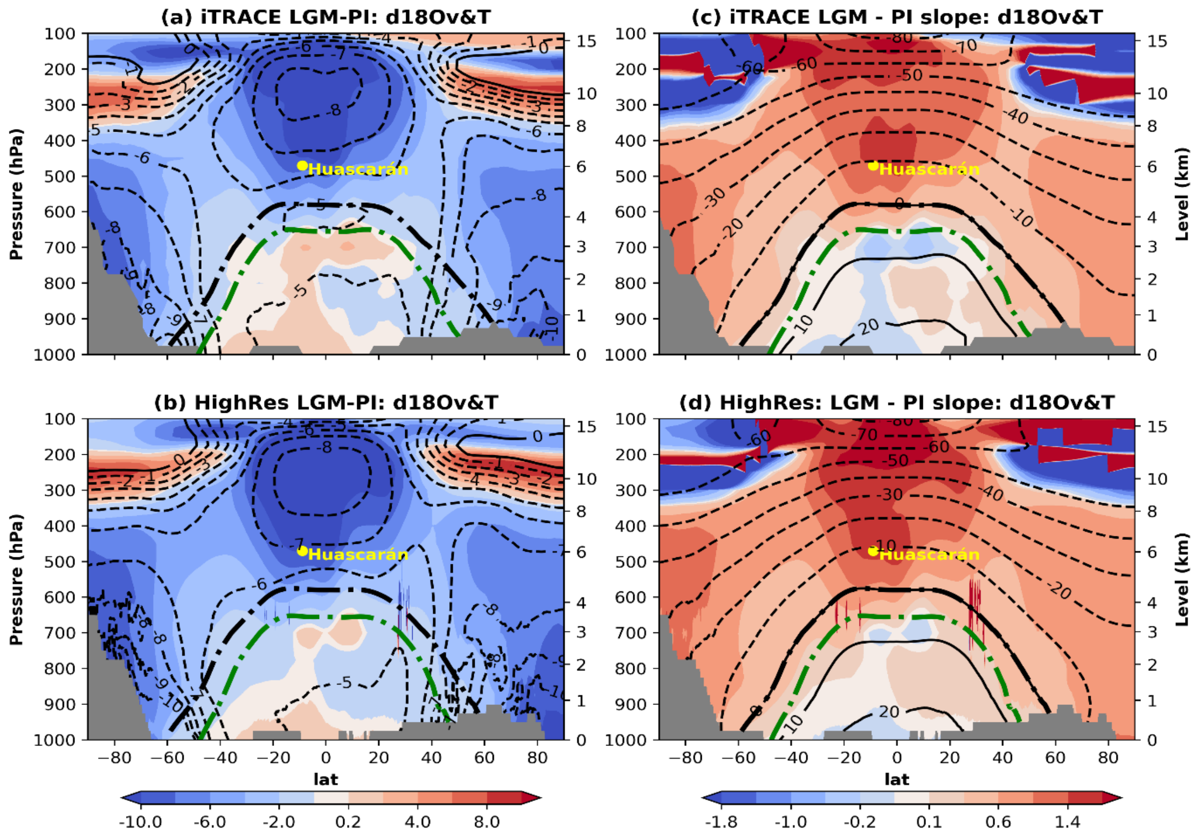

Fig. S6: Global zonal mean LGM-PI difference of model $\delta^{18}O_v$, temperature, and $d\delta^{18}O_v/dT$ slope: Zonal mean LGM – PI difference for $\delta^{18}O_v$ (shading, permil) and temperature (contour, °C) in (a) iTRACE model and b) HighRes model, and the resulted $\Delta\delta^{18}O_v/\Delta T$ slope in (c) iTRACE model and (d) HighRes model. Zonal mean climatology temperatures at the PI are also plotted in (c) and (d) (black contours). Heavy black and green dash dot lines are the zonal mean annual freezing level at the PI and the LGM, respectively. The real world Huascarán site is also marked.

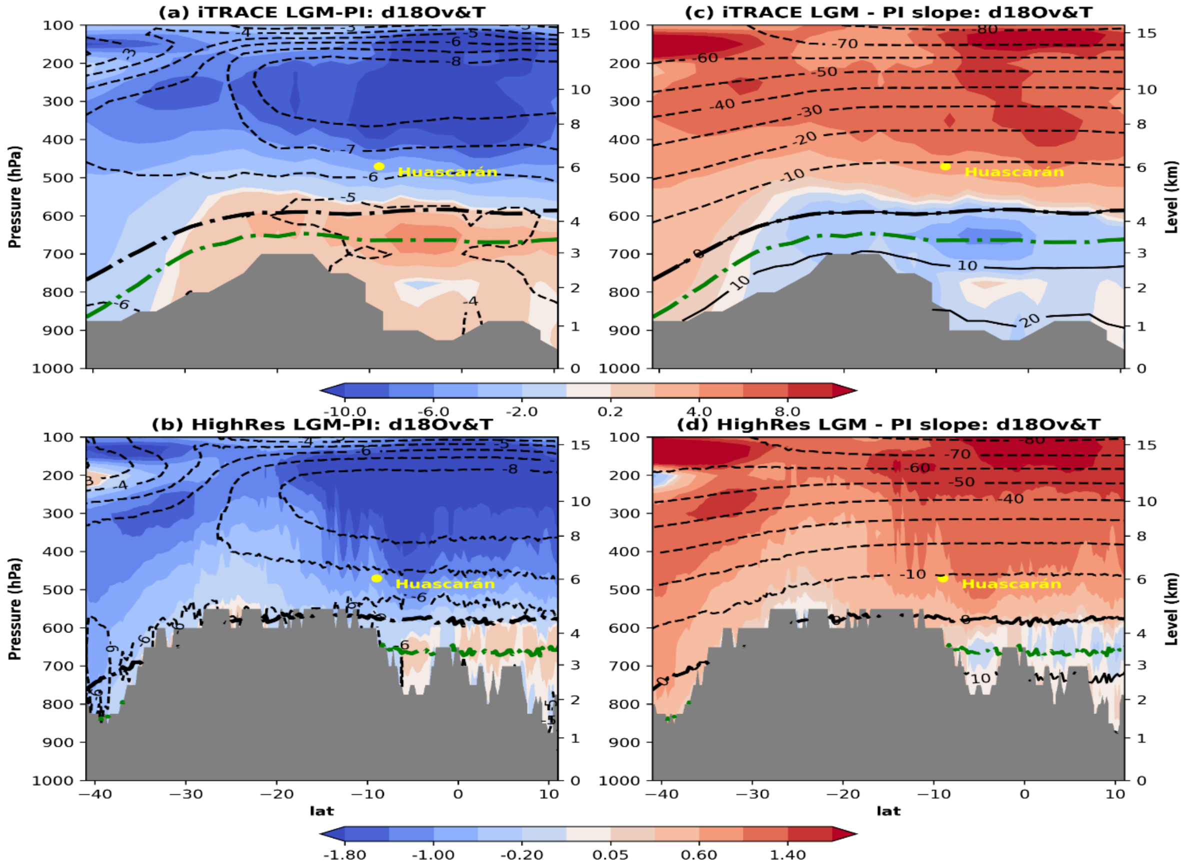

Fig. S7: LGM-PI difference of model $\delta^{18}O_v$, $temperature$, and $d\delta^{18}O_v/dT$ slope along the Andes: LGM – PI difference of $\delta^{18}O_v$ (shading, permil) and of the temperature (contour, °C) in (a) iTRACE and b) HighRes model along the Andes, and the resulting $\Delta\delta^{18}O_v/\Delta T$ slope (shading, permil/^oC) in (c) iTRACE model and (d) HighRes model. Climatology temperatures at the PI are also plotted in (c) and (d) (black contours). The heavy black and green dash dot lines in each panel are the annual freezing line ($0\,^oC$) for the PI and the LGM, respectively. The topography is the highest topography in this model section with the real world Huascarán site also marked.

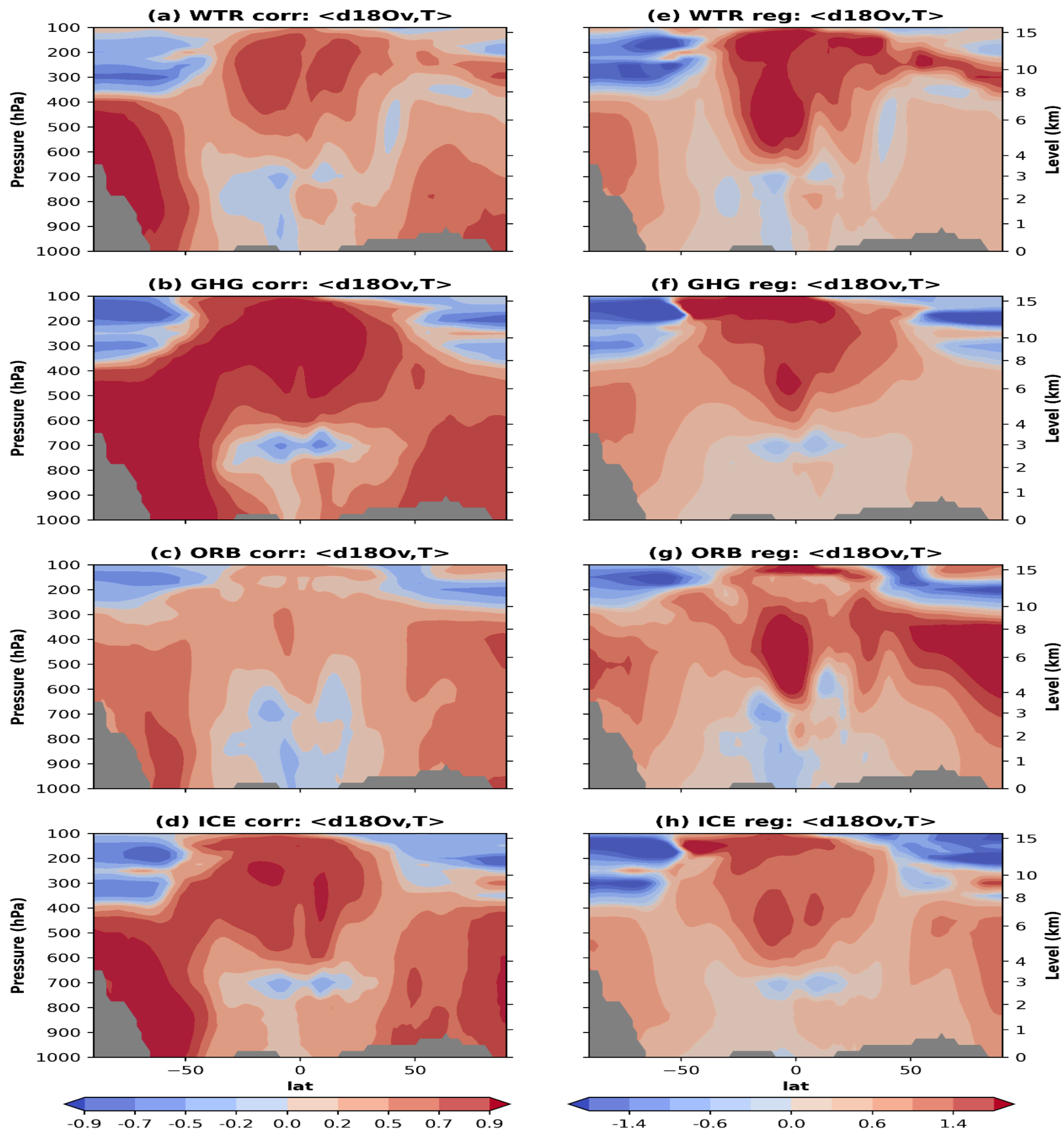

Fig. S8: Response to Individual Forcing in iTRACE: Zonal mean temporal correlation between $\delta^{18}O_v$ and temperature evolution during the last deglaciation (21-11ka) in response to different forcings from the iTRACE sensitivity experiments: (a) meltwater forcing (WTR); (b) greenhouse gases (GHG); (c) orbital (ORB); (d) icesheet (ICE). (e), (f), (g) and (h) are the same as (a), (b), (c) and (d), respectively, except for the $d\delta^{18}O_v/dT$ regression slope (shading, permil/^{o}C).

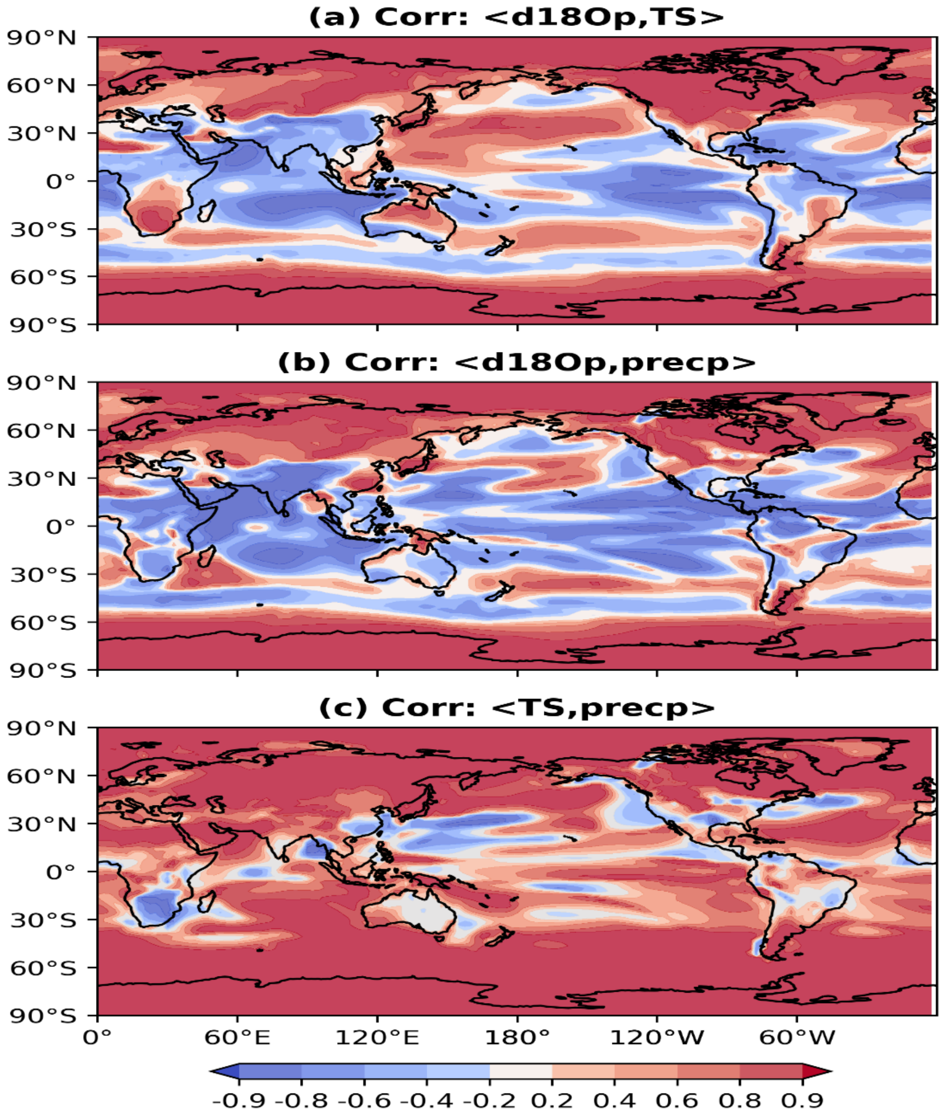

Fig. S9: Surface correlation maps during the last deglaciation from iTRACE: (a) cor $< \delta^{18}O_p, T_s >$: correlation between precipitation $\delta^{18}O_p$ and surface temperature. (b) $cor < \delta^{18}O_p, Prcp >$: correlation between $\delta^{18}O_p$ and precipitation. (c) cor $< T_s, Prcp >$: correlation between surface temperature and precipitation. All correlations are made between 21 and 11ka after creating 500-year running means.

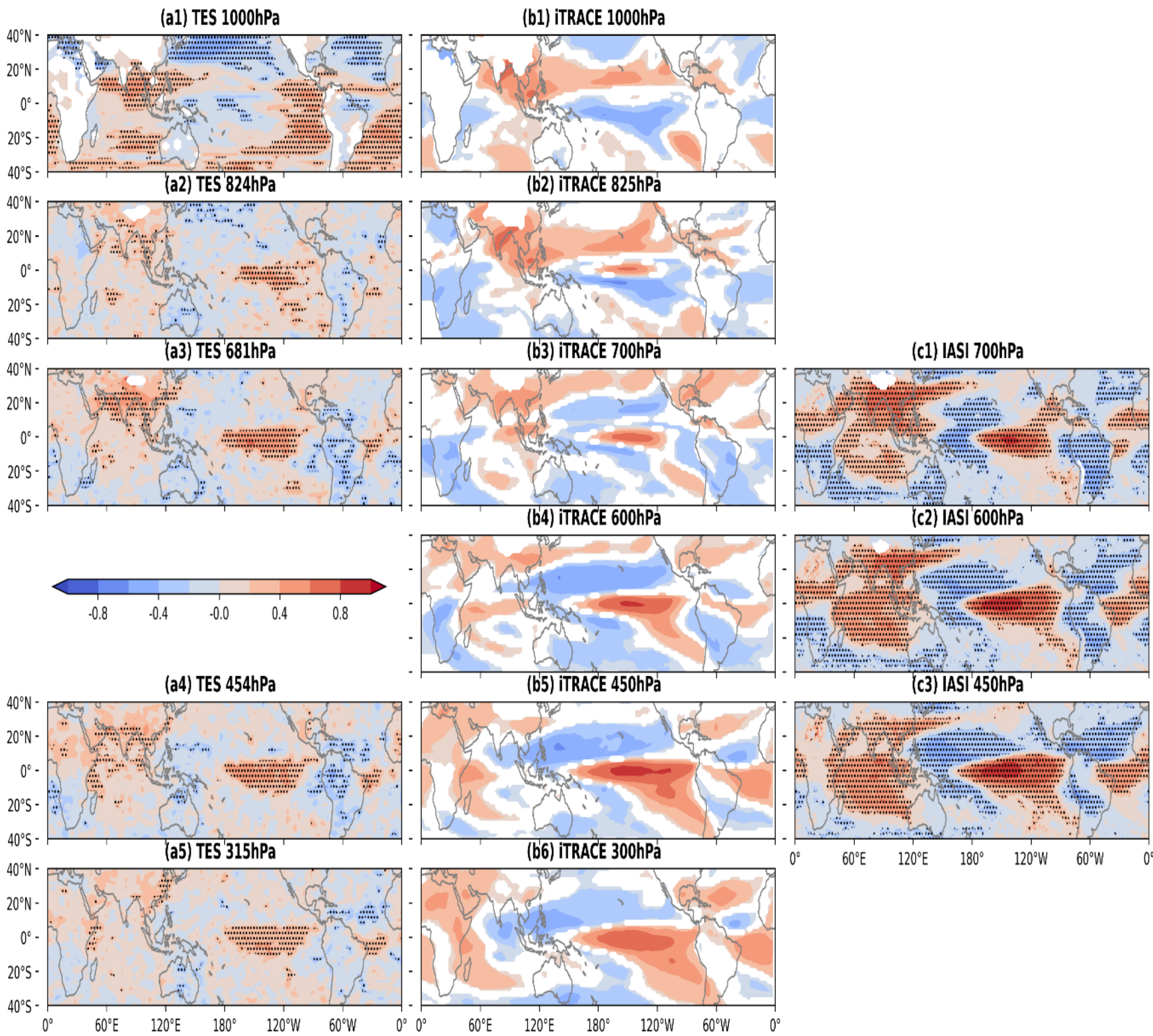

Fig. S10: Vertical structure of δD_v in response to ENSO: Correlation map between monthly Nino3 index and δD_v at different levels. (a1-a5): TES δD_v measurements of 2004 to 2012 on 5 levels. (b1-b6) iTRACE PI simulation, (similar in HighRes). (c1-c3) IASI δD_v measurements of 2014 to 2020 on 3 levels. Dotted region in (a) and (c) and colored region in (b) for correlations passing the 90% significance level.

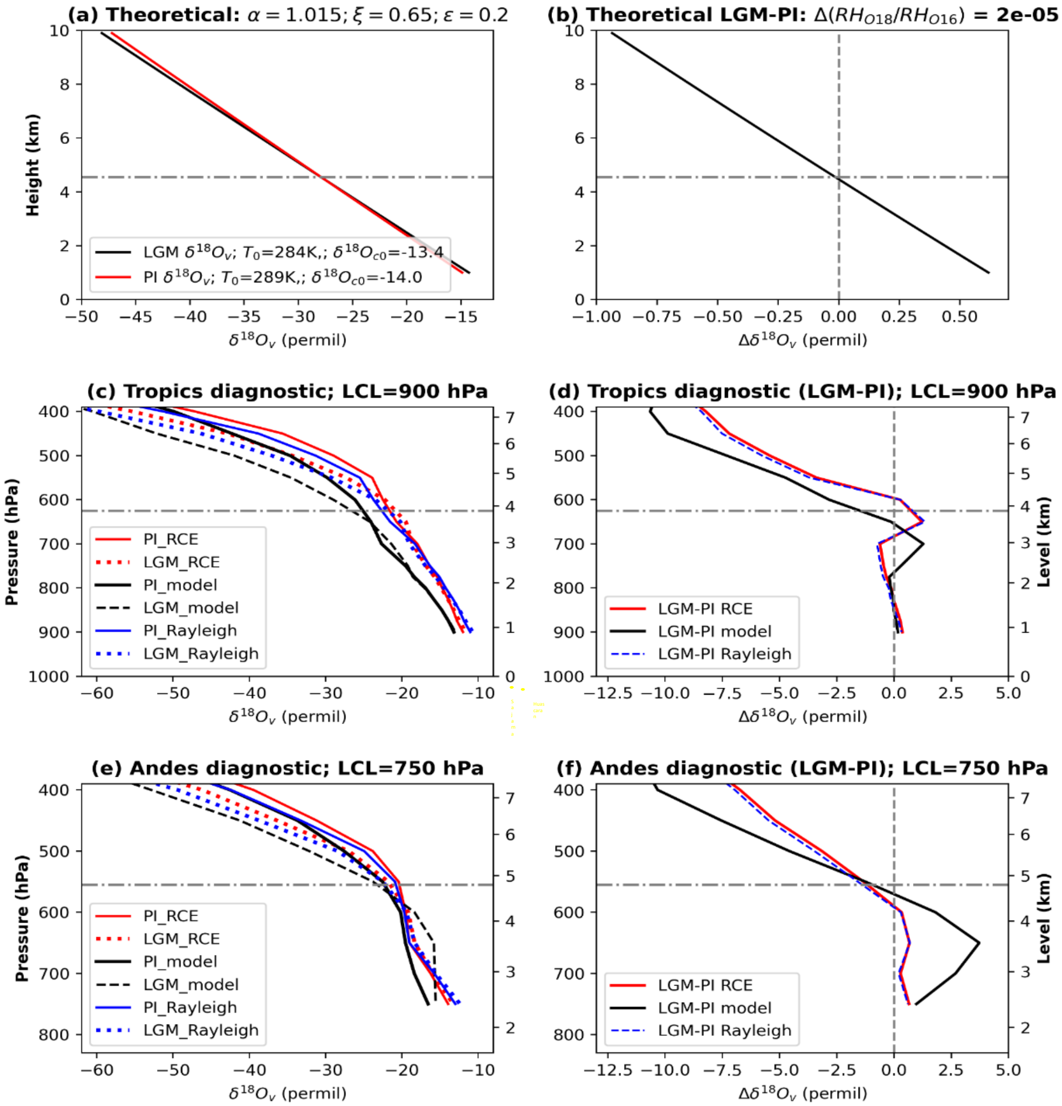

Fig. S11: Vertical profiles of $\delta^{18}O_v$ for PI and LGM. (a) Theoretical RCE solutions for a constant temperature lapse rate of Γ =6.4K/km, fractionation coefficient $\alpha = 1.015$, the reevaporation fraction $\xi = 0.65$ and distance $\Delta z = 0\ km,$ entrainment/detrainment rate ε= $\delta = 0.2 km^{-1}$. The red line is for the PI, with $\delta^{18}O_c(0) = -14.0$ permil, $T = 289K$. The black line is for the LGM, with $\delta^{18}O_c(0) = -13.4$ permil, T= $284K$. (b) $\delta^{18}O_v$ difference between LGM and PI of the two theoretical solutions in (a). (c) $\delta^{18}O_v$ over the tropics iTRACE PI (black solid) and LGM (black dash) compared with the theoretical solutions, in which the temperature lapse rate and temperature (in the calculation of water vapor lapse rates γ and γ') are diagnosed from iTRACE model in the RCE model (of ε, $\delta, \Delta z$ and ξ as in (a)) at PI (red solid) and LGM (red dash), and in the Rayleigh model at PI (blue solid) and LGM (blue dash). (d) $\delta^{18}O_v$ difference (LGM-PI) in iTRACE model (black) and the RCE model (red) and Rayleigh model (blue dash) diagnosed using iTRACE temperature as presented in (c). (e) and (f) are the same as (c) and (d) but for the Andes region. The LCL (lifting condensation level) are calculated using model variables, and serves as the cloud base, above which the RCE and Rayleigh models are applied.

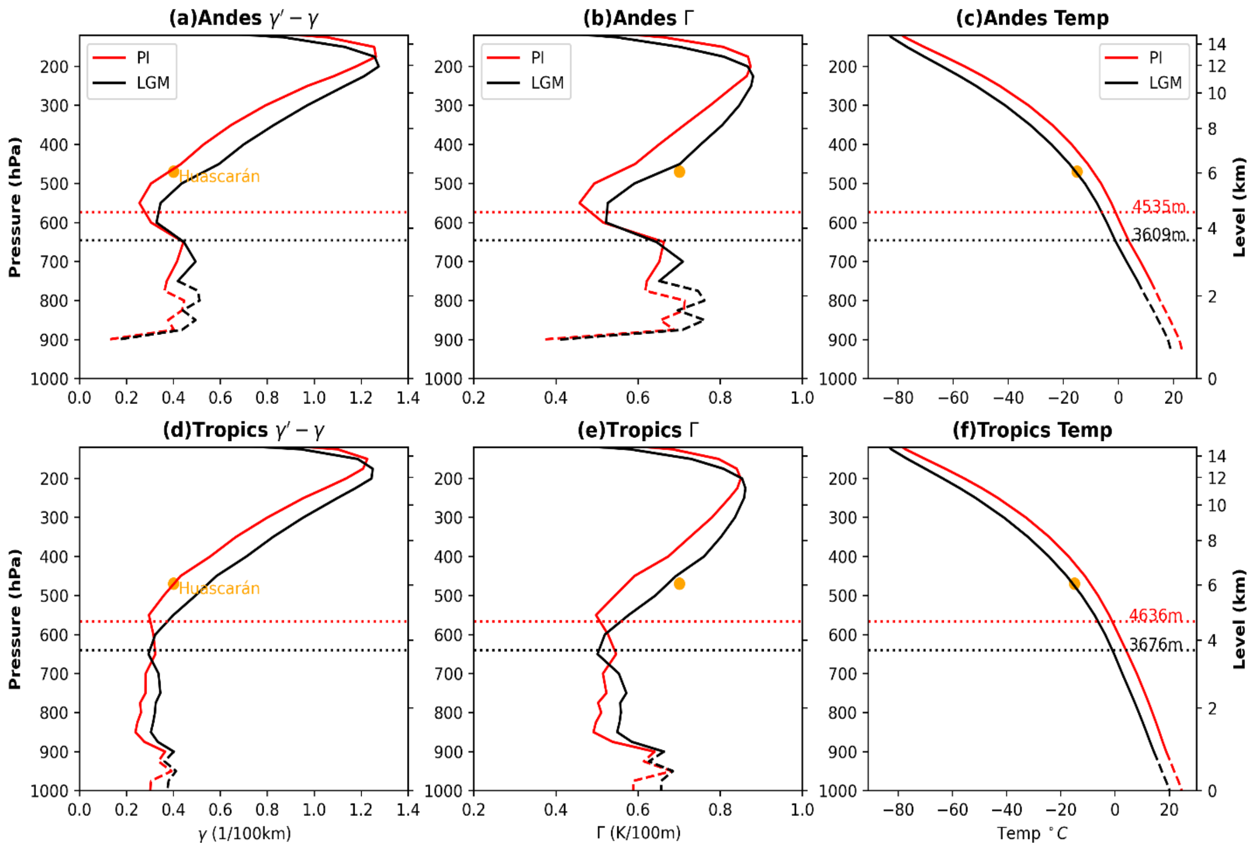

Fig. S12: Vertical profiles of lapse rates and temperature in iTRACE: Vertical profiles of (a) the depletion rate of $\delta^{18}O_v(z)$ as the difference between the lapse rates of ^{18}O (γ') and ^{16}O (γ) (γ' -γ, in 1/100km), (b) environmental temperature lapse rate ($\Gamma = °\mathrm{C}/100m$) and (c) temperature (°C) diagnosed from iTRACE simulations at PI (red) and LGM (black) over the Andean region. (d-f) are the same as (a-c) but for the entire tropics 20S-20N. The annual freezing levels are also marked in (c) and (f).

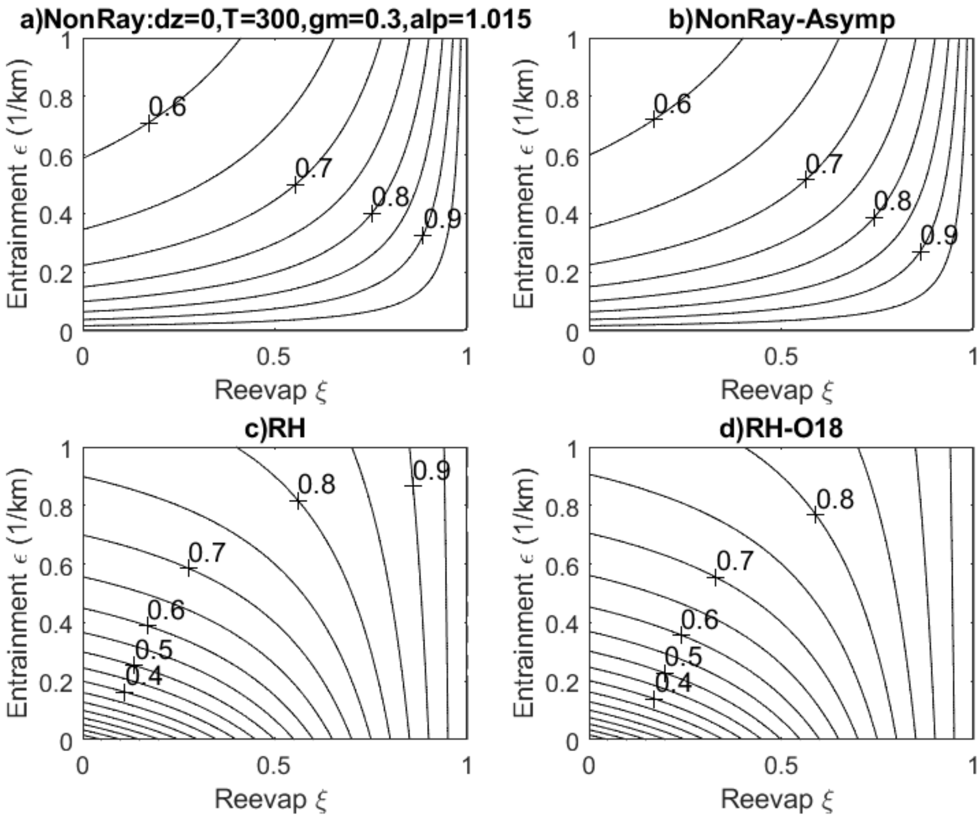

Fig.S13: RCE model solution: as functions of entrainment/detrainment rate ε (1/km) and re-evaporation efficiency ξ. The Non-Rayleigh factor N is solved numerically for (a) the full solution (eqn. (7)) and (b) the asymptotic solution (eqn. (10-11)), with the relative humidity for (c) moisture and (d) isotope from the full solution. Other model parameters are $T \ = 300$K, $\alpha = 1.015$, $\Delta z = 0$ km, Γ=7 K/km.

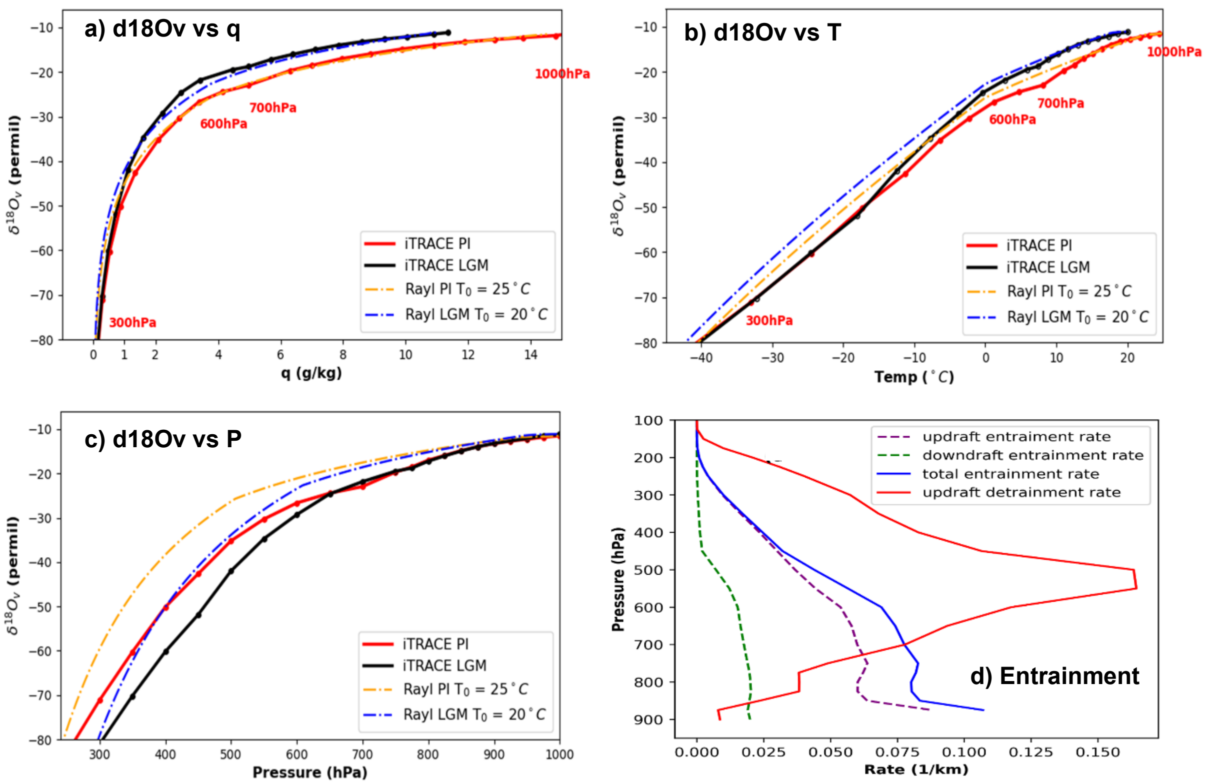

Fig.S14: Tropical mean moisture and isotopes in iCESM. (a) $\delta^{18}O_v$ as a function of specific humidity q in iTRACE at PI (red) and LGM (black), and in the Rayleigh model for PI (orange) and LGM (blue), with some pressure levels marked for PI in iTRACE. (b) Same as (a) but for $\delta^{18}O_v$ as a function of saturation temperature. (c) Same as (a) but for $\delta^{18}O_v$ as a function of pressure (height) in which the temperature is converted to pressure using iTRACE output. (d) Vertical profiles of total entrainment (blue), its downdraft (green) and updraft (purple) components, and total detrainment (red) in the PI simulation.

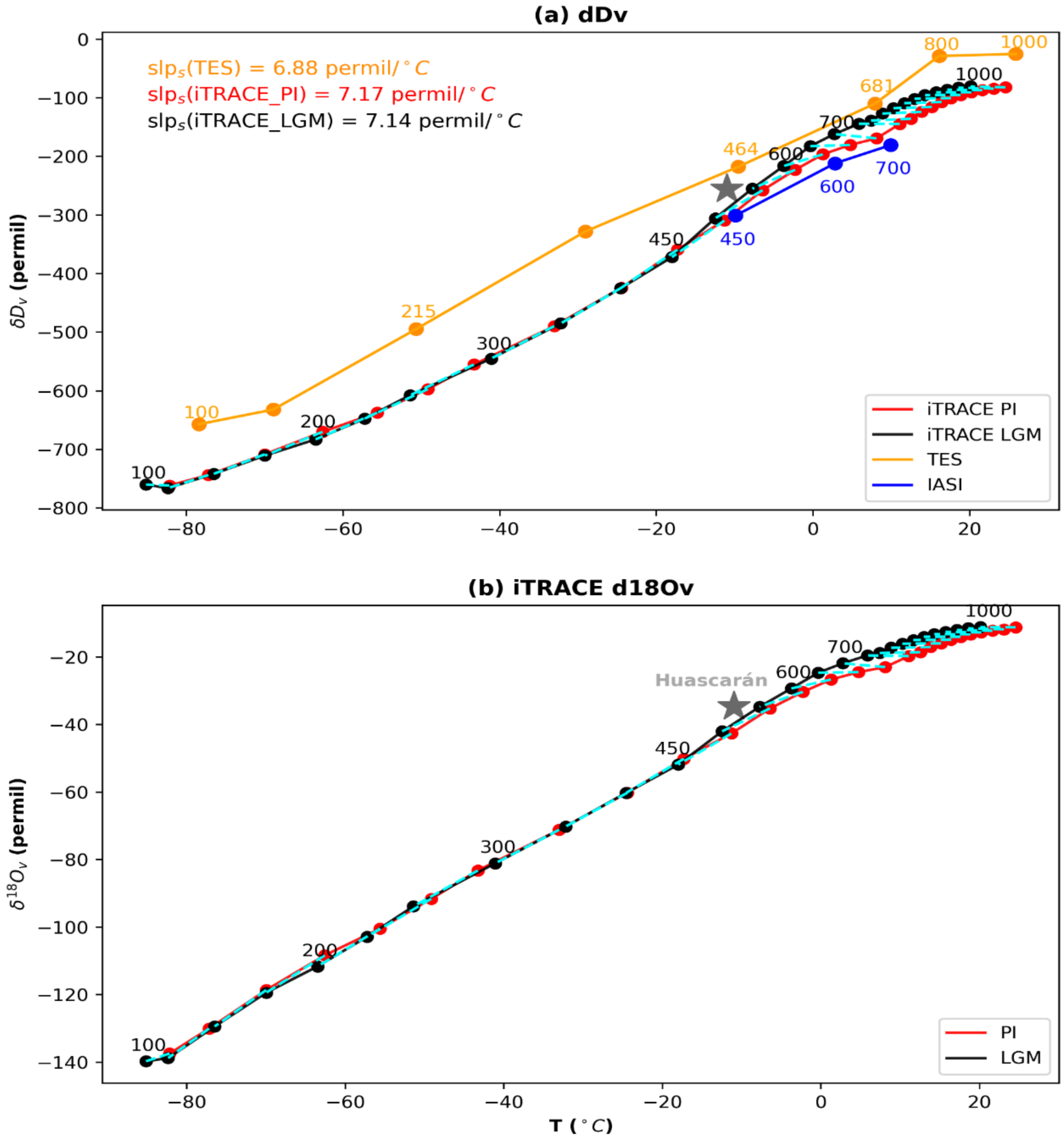

Fig. S15: Spatial and temporal slope in the tropics. (a) δD_v and temperature at different levels in TES (yellow), IASI (blue), iTRACE PI (red) and LGM (black). The cyan dash that connects iTRACE LGM and PI of the same level can be considered as the deglacial temporal slope. (b) The same as in (a) for iTRACE PI and LGM, but for $\delta^{18}O_v$. The value of spatial slopes and temporal slopes in (b) are calculated for 650 hPa to 150hPa in iTRACE and from 800 hPa to 150 hPa for TES. The star in a and b represents the height of Huascarán.

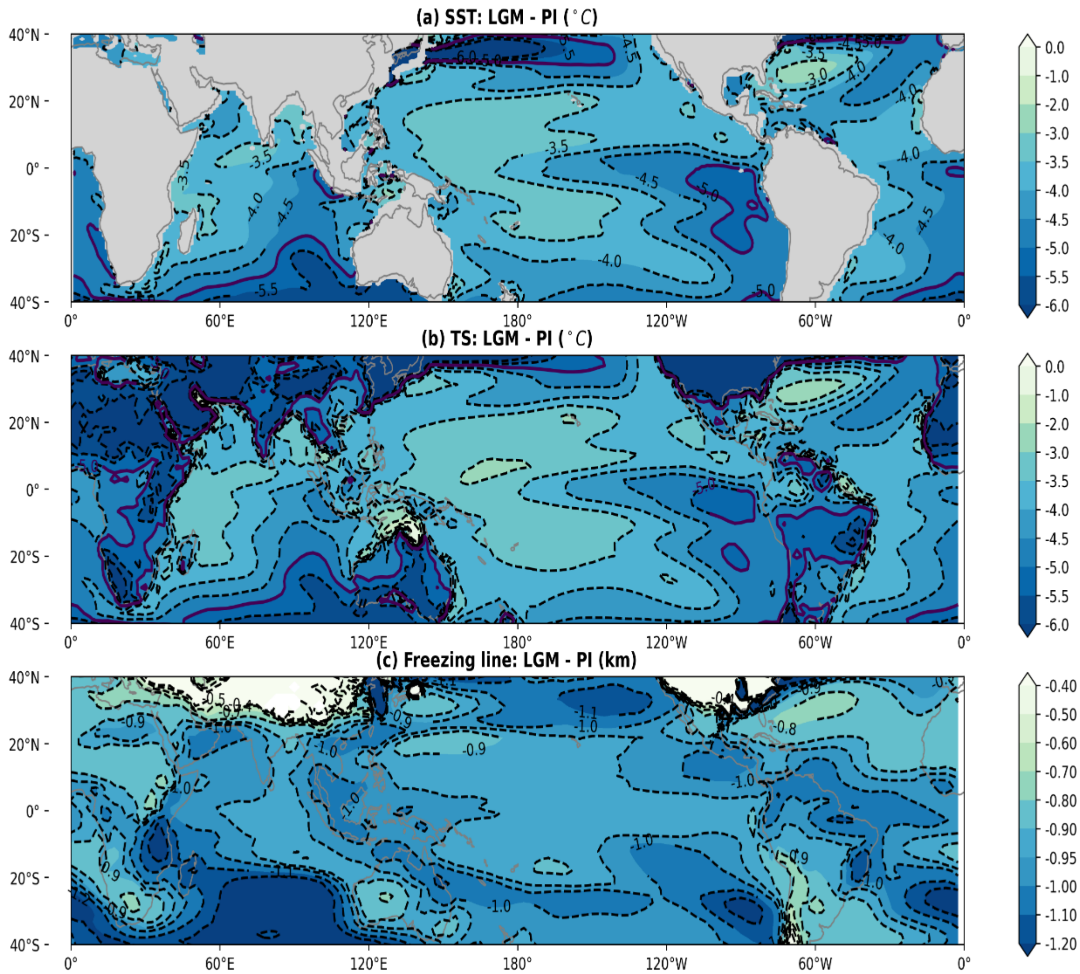

Fig. S16: Difference map between LGM and PI. (a) sea surface temperature (°C); (b) surface temperature (°C); (c) freezing line (km)

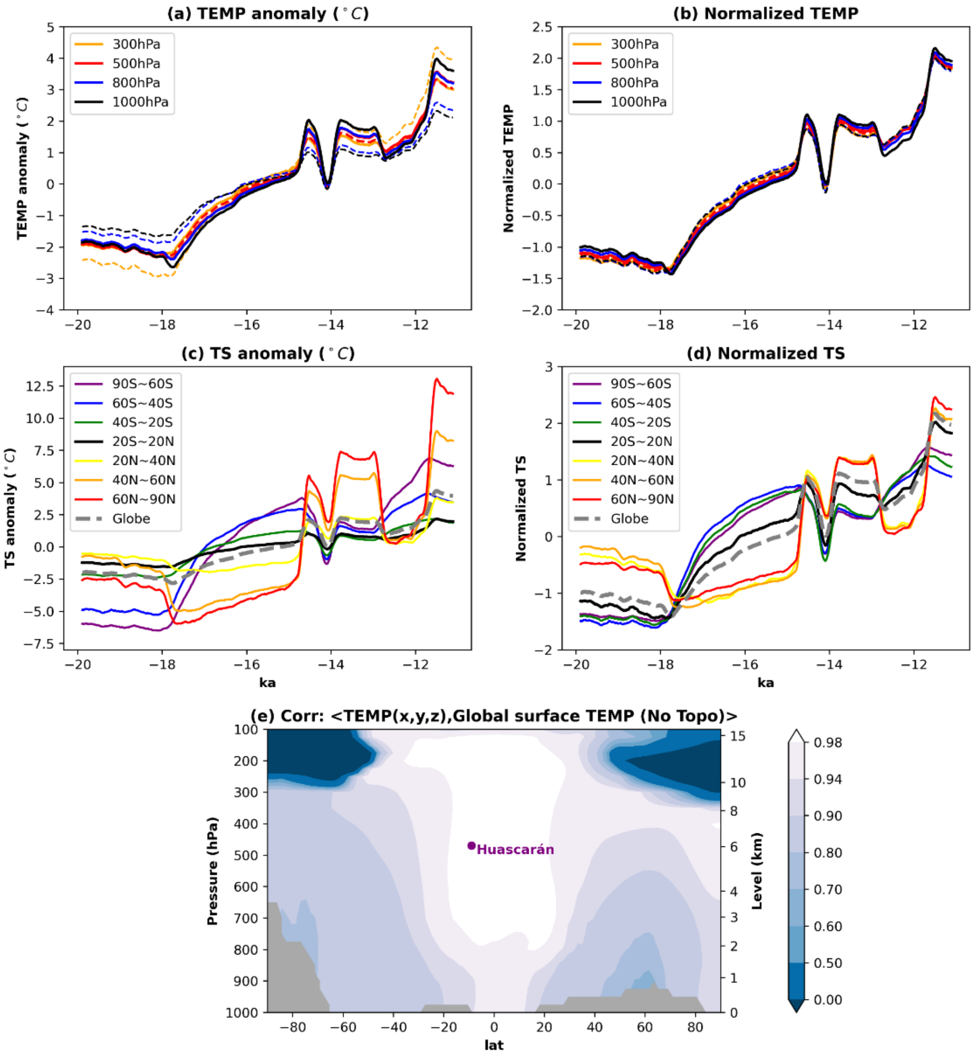

Fig. S17: Evolution of air temperature anomaly (from the long term mean) in iTRACE. (a) Annual mean air temperature anomaly (°C) at 1000, 800, 500 and 300 hPa averaged in the tropics (20ºS-20ºN, dash) and for the globe (solid). (b) Same as (a) but each temperature anomaly is normalized by its standard deviation. (c) Annual mean surface (1000 hPa) air temperature anomaly (°C) in different latitude bands. (d) Same as (c) but each temperature is normalized by its standard deviation. (e) Zonal mean correlation of atmospheric temperature at each grid point against the global mean surface temperature from 20ka to 11ka. In (c)-(e), the surface temperature under topography is calculated after extrapolation to 1000 hPa using the dry lapse rate (No-TOPO). These figures show that temperature evolution at Huascarán (approximately the 500 hPa tropical temperature in (a) and (b)) resembles well that in the tropics at different levels as well as the global mean temperature in the lower atmosphere.

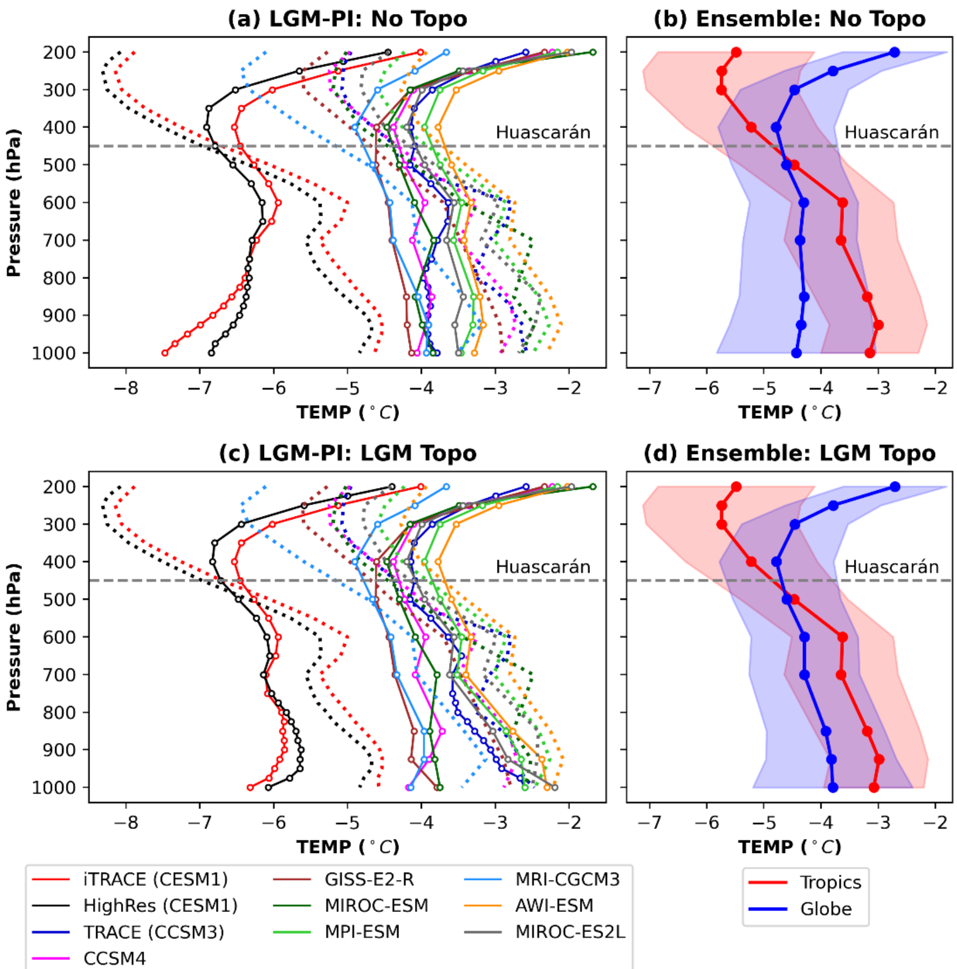

Fig. S18: Vertical Profile of Temperature Response in climate models (a) Vertical profile of LGM-PI annual mean air temperature difference (°C) averaged in the tropics (20S-20N, dot) and globe (solid) for iTRACE, HighRes, PMIP3 and PMIP4 models. (For clarify, PMIP2 are not shown here, but shown in Fig.S19). (b) The ensemble mean (solid) and spread (shading) of the vertical profiles across all the models in (a) for the tropical (red) and global (blue) mean. The global mean temperature field is extrapolated below model topography to 1000 hPa using a dry lapse rate of 10°C /100 hPa (No-Topo). (c) and (d) are respectively the same as (a) and (b), but for the temperature above the LGM topography only (LGM-Topo). The magnitude of temperature change in the tropical mid-troposphere (as for the Huascarán ice core, grey dash), although greater than below locally in the tropics, is about the same as that of the global mean temperature change at this level and below. Thus, the Huascarán ice core also provides a good quantitative indicator of global temperature change in the lower atmosphere.

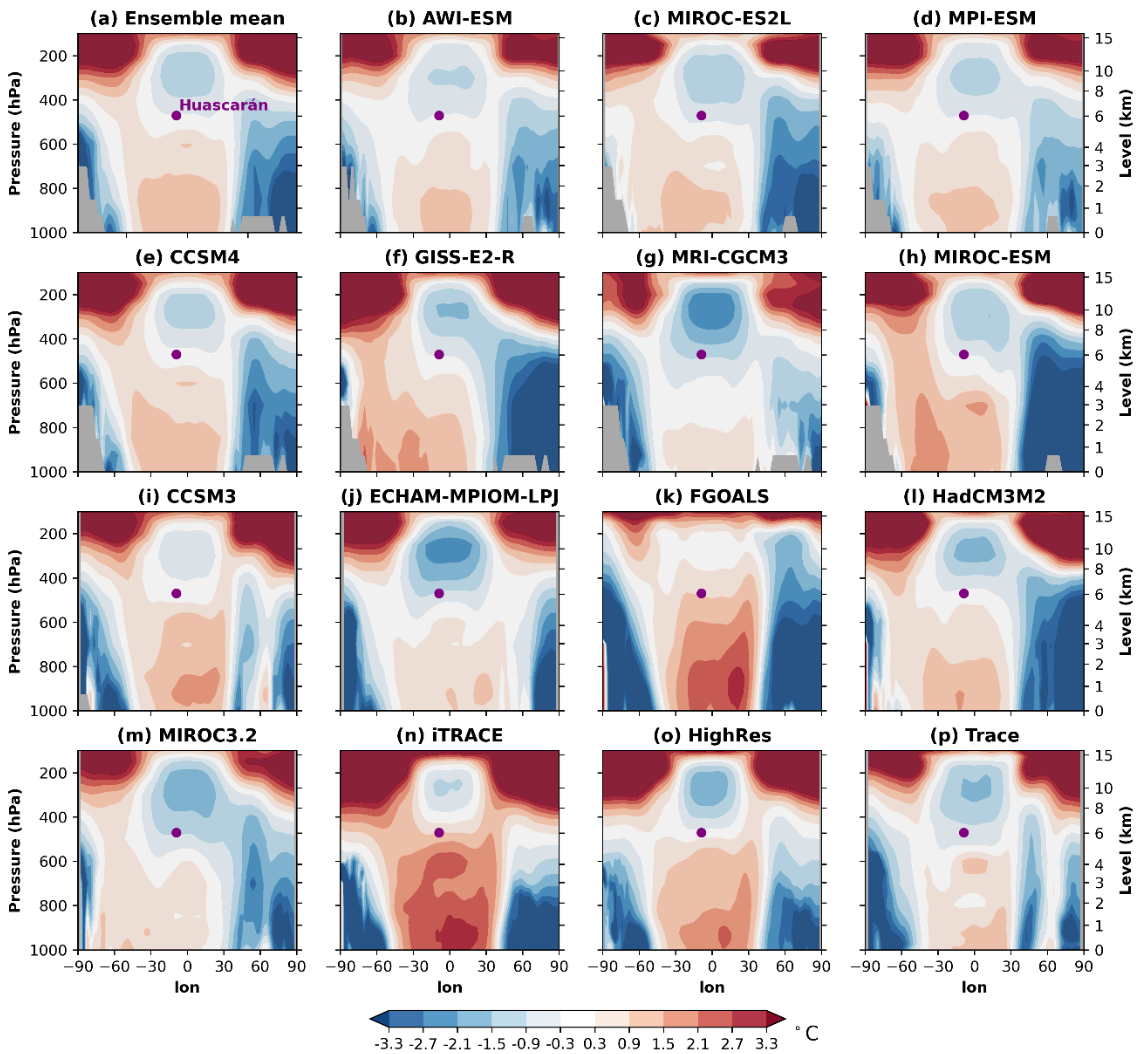

Fig. S19: Difference of LGM-PI temperature change from GMST change. Zonal mean difference of the LGM-PI temperature response at each grid point from the GMST response (No-Topo) in each PMIP model, iTRACE, HighRes and the ensemble mean. In most models, the Huascarán ice core site appears to occupy the Goldilocks position of minimum deviation.

REFERENCES AND NOTES

1. L. G. Thompson, Glaciological investigations of the tropical Quelccaya ice Cap, Peru. *J. Glaciol.* **25**, 69–84 (1980).

2. L. G. Thompson, E. Mosley-Thompson, B. M. Arnao, El Niño-southern Oscillation events recorded in the stratigraphy of the tropical Quelccaya ice cap, Peru. *Science* **226**, 50–53 (1984).

3. L. G. Thompson, E. Mosley-Thompson, M. E. Davis, P.-N. Lin, K. A. Henderson, J. Cole-Dai, J. F. Bolzan, K.-B. Liu, Late glacial stage and Holocene tropical ice core records from Huascarán, Peru. *Science* **269**, 46–50 (1995).

4. L. G. Thompson, T. Yao, M. Davis, K. Henderson, E. Mosley-Thompson, P.-N. Lin, J. Beer, H.-A. Synal, J. Cole-Dai, J. Bolzan, Tropical climate instability: The last glacial cycle from a Qinghai-Tibetan ice core. *Science* **276**, 1821–1825 (1997).

5. L. G. Thompson, M. E. Davis, E. Mosley-Thompson, T. A. Sowers, K. A. Henderson, V. S. Zagorodnov, P.-N. Lin, V. N. Mikhalenko, R. K. Campen, J. F. Bolzan, A 25,000-year tropical climate history from Bolivian ice cores. *Science* **282**, 1858–1864 (1998).

6. L. G. Thompson, E. Mosley-Thompson, M. E. Davis, K. A. Henderson, H. H. Brecher, V. S. Zagorodnov, T. A. Mashiotta, P.-N. Lin, V. N. Mikhalenko, D. R. Hardy, J. Beer, Kilimanjaro ice core records: Evidence of Holocene climate change in tropical Africa. *Science* **298**, 589–593 (2002).

7. B. W. Bird, M. B. Abbott, M. Vuille, D. T. Rodbell, N. D. Stansell, M. F. Rosenmeier, A 2,300-year-long annually resolved record of the South American summer monsoon from the Peruvian Andes. *Proc. Natl. Acad. Sci. U.S.A.* **108**, 8583–8588 (2011).

8. M. Vuille, S. J. Burns, B. L. Taylor, F. W. Cruz, B. W. Bird, M. B. Abbott, L. C. Kanner, H. Cheng, V. F. Novello, A review of the South American monsoon history as recorded in stable isotopic proxies over the past two millennia. *Clim. Past.* **8**, 1309–1321 (2012).

9. W. Dansgaard, Stable isotopes in precipitation. *Tellus* **16**, 436–468 (1964).

10. J. Jouzel, F. Vimeux, N. Caillon, G. Delaygue, G. Hoffmann, V. Masson-Delmotte, F. Parrenin, Magnitude of isotope/temperature scaling for interpretation of central Antarctic ice cores. *J. Geophys. Res. Atmos.* **108**, 10.1029/2002JD002677 (2003).

11. R. B. Alley, K. M. Cuffey, Oxygen- and hydrogen-isotopic ratios of water in precipitation: Beyond paleothermometry. *Rev. Mineral. Geochem.* **43**, 527–553 (2001).

12. K. Cuffey, W. S. B. Paterson, *"Ice Core Studies" in The physics of glaciers* (Academic Press, 2010), 645–647.

13. Y. J. Wang, H. Cheng, R. L. Edwards, Z. An, J. Y Wu, C.-C. Shen, J. A. Dorale, A high-resolution absolute-dated late Pleistocene monsoon record from Hulu Cave, China. *Science* **294**, 2345–2348 (2001).

14. F. S. R. Pausata, D. S. Battisti, K. H. Nisancioglu, C. M. Bitz, Chinese stalagmite $\delta^{18}O$ controlled by changes in the Indian monsoon during a simulated Heinrich event. *Nat. Geosci.* **4**, 474–480 (2011).

15. Z. Liu, X. Wen, E. C Brady, B. Otto-Bliesner, G. Yu, H. Lu, H. Cheng, Y. Wang, W. Zheng, Y. Ding, R. L. Edwards, J. Cheng, W. Liu, H. Yang, Chinese cave records and the East Asia summer monsoon. *Quat. Sci. Rev.* **83**, 115–128 (2014).

16. X. Liu, D. S. Battisti, The influence of orbital forcing of tropical insolation on the climate and isotopic composition of precipitation in South America. *J. Climate* **28**, 4841–4862 (2015).

17. J. C. H. Chiang, I. Y. Fung, C.-H. Wu, Y. Cai, J. P. Edman, Y. Liu, J. A. Day, T. Bhattacharya, Y. Mondal, C. A. Labrousse, Role of seasonal transitions and westerly jets in East Asian paleoclimate. *Quat. Sci. Rev.* **108**, 111–129 (2015).

18. C. He, Z. Liu, B. Otto-Bliesner, E. Brady, C. Zhu, R. Tomas, P. U. Clark, J. Zhu, A. Jahn, S. Gu, J. Zhang, J. Nusbaumer, D. Noone, Y. Wang, M. Yan, Y. Bao, Hydroclimate footprint of pan-Asian monsoon water isotope during the last deglaciation. *Sci. Adv.* **7**, eabe2611 (2021).

19. Y. Bao, Z. Liu, C. He, Dipole response of millennial variability in tropical South American precipitation and $\delta^{18}O_p$ during the last deglaciation: Part I: Rainfall response. *J. Climate* **36**, 4691–4707 (2023).

20. Y. Bao, Z. Liu, C. He, Dipole response of millennial variability in tropical South American precipitation and $\delta^{18}O_p$ during the last deglaciation: Part II: $\delta^{18}O_p$ response. *J. Climate* **36**, 4709–4721 (2023).

21. C. Risi, S. Bony, F. Vimeux, Influence of convective processes on the isotopic composition ($\delta^{18}O$ and δD) of precipitation and water vapor in the tropics: 2. Physical interpretation of the amount effect. *J. Geophys. Res. Atmos.* **113**, 10.1029/2008JD009943 (2008).

22. M. Vuille, R. S. Bradley, R. Healy, M. Werner, D. R. Hardy, L. G. Thompson, F. Keimig, Modeling $\delta^{18}O$ in precipitation over the tropical Americas: 2. Simulation of the stable isotope signal in Andean ice cores. *J. Geophys. Res. Atmos.* **108**, 10.1029/2001JD002039 (2003).

23. W. S. Broecker, Mountain glaciers: Recorders of atmospheric water vapor content? *Global Biogeochem. Cycles* **11**, 589–597 (1997).

24. R. T. Pierrehumbert, Huascaran $\delta^{18}O$ as an indicator of tropical climate during the Last Glacial Maximum. *Geophys. Res. Lett.* **26**, 1345–1348 (1999).

25. P. A. Baker, C. A. Rigsby, G. O. Seltzer, S. C. Fritz, T. K. Lowenstein, N. P. Bacher, C. Veliz, Tropical climate changes at millennial and orbital timescales on the Bolivian Altiplano. *Nature* **409**, 698–701 (2001).

26. E. Ramirez, G. Hoffmann, J. D. Taupin, B. Francou, P. Ribstein, N. Caillon, F. Ferron, A. Landais, J. Petit, B. Pouyaud, U. Schotterer, J. C. Simoes, M. Stievenard, A new Andean deep ice core from Nevado Illimani (6350 m), Bolivia. *Earth Planet. Sci. Lett.* **212**, 337–350 (2003).

27. M. Vuille, M. Werner, Stable isotopes in precipitation recording South American summer monsoon and ENSO variability: Observations and model results. *Clim. Dynam.* **25**, 401–413 (2005).

28. K. E. Samuels-Crow, J. Galewsky, D. R. Hardy, Z. D. Sharp, J. Worden, C. Braun, Upwind convective influences on the isotopic composition of atmospheric water vapor over the tropical Andes. *J. Geophys. Res. Atmos.* **119**, 7051–7063 (2014).

29. P. G. Aron, C. J. Poulsen, R. P. Fiorella, N. E. Levin, R. P. Acosta, B. J. Yanites, E. J. Cassel, Variability and controls on $\delta^{18}O$, d-excess, and $\Delta'\,^{17}O$ in Southern Peruvian precipitation. *J. Geophys. Res. Atmos.* **126**, e2020JD034009 (2021).

30. R. P. Fiorella, C. J. Poulsen, R. S. Pillco Zola, J. B. Barnes, C. R. Tabor, T. A. Ehlers, Spatiotemporal variability of modern precipitation $\delta^{18}O$ in the central Andes and implications for paleoclimate and paleoaltimetry estimates. *J. Geophys. Res. Atmos.* **120**, 4630–4656 (2015).

31. H. Guy, A. Seimon, L. B. Perry, B. L. Konecky, M. Rado, M. Andrade, M. Potocki, P. A. Mayewski, Subseasonal variations of stable isotopes in tropical Andean precipitation. *J. Hydrometeorol.* **20**, 915–933 (2019).

32. N. Insel, C. J. Poulsen, C. Sturm, T. A. Ehlers, Climate controls on Andean precipitation $\delta^{18}O$ interannual variability. *J. Geophys. Res. Atmos.* **118**, 9721–9742 (2013).

33. F. Vimeux, R. Gallaire, S. Bony, G. Hoffmann, J. C. H. Chiang, What are the climate controls on δD in precipitation in the Zongo Valley (Bolivia)? Implications for the Illimani ice core interpretation. *Earth Planet. Sci. Lett.* **240**, 205–220 (2005).

34. F. Vimeux, G. Tremoy, C. Risi, R. Gallaire, A strong control of the South American SeeSaw on the intra-seasonal variability of the isotopic composition of precipitation in the Bolivian Andes. *Earth Planet. Sci. Lett.* **307**, 47–58 (2011).

35. L. R. Welp, E. J. Olson, A. L. Valdivia, J. R. Larico, E. P. Arhuire, L. M. Paredes, J. T. DeGraw, G. M. Michalski, Reinterpreting precipitation stable water isotope variability in the Andean Western Cordillera due to sub-seasonal moisture source changes and sub-cloud evaporation. *Geophys. Res. Lett.* **49**, e2022GL099876 (2022).

36. N. Insel, C. J. Poulsen, T. A. Ehlers, Influence of the Andes Mountains on South American moisture transport, convection, and precipitation. *Clim. Dynam.* **35**, 1477–1492 (2010).

37. C. J. Poulsen, T. A. Ehlers, N. Insel, Onset of convective rainfall during gradual late Miocene rise of the central Andes. *Science* **328**, 490–493 (2010).

38. J. L. Conroy, D. Noone, K. M. Cobb, J. W. Moerman, B. L. Konecky, Paired stable isotopologues in precipitation and vapor: A case study of the amount effect within western tropical Pacific storms. *J. Geophys. Res. Atmos.* **121**, 3290–3303 (2016).

39. S. Bony, C. Risi, F. Vimeux, Influence of convective processes on the isotopic composition ($\delta^{18}O$ and δD) of precipitation and water vapor in the tropics: 1. Radiative-convective equilibrium and Tropical Ocean–Global Atmosphere–Coupled Ocean-Atmosphere Response Experiment (TOGA-COARE) simulations. *J. Geophys. Res. Atmos.* **113**, 10.1029/2008JD009942 (2008.

40. L. C. Kanner, S. J. Burns, H. Cheng, R. L. Edwards, High-latitude forcing of the South American summer monsoon during the last glacial. *Science* **335**, 570–573 (2012).

41. V. F. Novello, F. W. Cruz, M. Vuille, N. M. Stríkis, R. L. Edwards, H. Cheng, S. Emerick, M. S. De Paula, X. Li, E. de S. Barreto, I. Karmann, R. V. Santos, A high-resolution history of the South American Monsoon from last glacial maximum to the Holocene. *Sci. Rep.* **7**, 44267 (2017).

42. J. Zhu, Z. Liu, E. C. Brady, B. L. Otto-Bliesner, S. A. Marcott, J. Zhang, X. Wang, J. Nusbaumer, T. E. Wong, A. Jahn, D. Noone, Investigating the direct meltwater effect in terrestrial oxygen-isotope paleoclimate records using an isotope-enabled Earth system model. *Geophys. Res. Lett.* **44**, 12501–12510 (2017).

43. J. Worden, K. Bowman, D. Noone, R. Beer, S. Clough, A. Eldering, B. Fisher, A. Goldman, M. Gunson, R. Herman, S. S. Kulawik, M. Lampel, M. Luo, G. Osterman, C. Rinsland, C. Rodgers, S. Sander, M. Shephard, H. Worden, Tropospheric emission spectrometer observations of the tropospheric HDO/H_2O ratio: Estimation approach and characterization. *J. Geophys. Res. Atmos.* **111**, 10.1029/2005JD006606 (2006).

44. J. Worden, S. Kulawik, C. Frankenberg, V. Payne, K. Bowman, K. Cady-Peirara, K. Wecht, J. E. Lee, D. Noone, Profiles of CH4, HDO, H2O, and N2O with improved lower tropospheric vertical resolution from Aura TES radiances. *Atmospheric Meas. Tech.* **5**, 397–411 (2012).

45. C. J. Diekmann, M. Schneider, B. Ertl, F. Hase, O. García, F. Khosrawi, E. Sepúlveda, P. Knippertz, P. Braesicke, The global and multi-annual MUSICA IASI {H2O, δD} pair dataset. *Earth Syst. Sci. Data* **13**, 5273–5292 (2021).

46. S. Sutanto, G. Hoffmann, J. Worden, R. Scheepmaker, I. Aben, T. Roeckmann, Atmospheric processes governing the changes in water isotopologues during ENSO events from model and satellite measurements. *J. Geophys. Res. Atmos.* **120**, 6712–6729 (2015).

47. D. M. Romps, An analytical model for tropical relative humidity. *J. Climate* **27**, 7432–7449 (2014).

48. S. Q. Duan, J. S. Wright, D. M. Romps, On the utility (or futility) of using stable water isotopes to constrain the bulk properties of tropical convection. *J. Adv. Model. Earth Syst.* **10**, 516–529 (2018).

49. Z. Kuang, G. C. Toon, P. O. Wennberg, Y. L. Yung, Measured HDO/H_2O ratios across the tropical tropopause. *Geophys. Res. Lett.* **30**, 10.1029/2003GL017023 (2003).

50. J. Worden, D. Noone, K. Bowman; The Tropospheric Emission Spectrometer science team and data contributors, Importance of rain evaporation and continental convection in the tropical water cycle. *Nature* **445**, 528–532 (2007).

51. J.-E. Lee, I. Fung, "Amount effect" of water isotopes and quantitative analysis of post-condensation processes. *Hydrol. Process.* **22**, 1–8 (2008).

52. C. S. Bretherton, A. H. Sobel, The Gill model and the weak temperature gradient approximation. *J. Atmos. Sci.* **60**, 451–460 (2003).

53. D. Rind, D. Peteet, Terrestrial conditions at the Last Glacial Maximum and CLIMAP sea-surface temperature estimates: Are they consistent? *Quatern. Res.* **24**, 1–22 (1985).

54. A. G. Klein, G. O. Seltzer, B. L. Isacks, Modern and last local glacial maximum snowlines in the Central Andes of Peru, Bolivia, and Northern Chile. *Quat. Sci. Rev.* **18**, 63–84 (1999).

55. S. C. Porter, Snowline depression in the tropics during the Last Glaciation. *Quat. Sci. Rev.* **20**, 1067–1091 (2000).

56. A. M. Seltzer, J. Ng, W. Aeschbach, R. Kipfer, J. T. Kulongoski, J. P. Severinghaus, M. Stute, Widespread six degrees Celsius cooling on land during the Last Glacial Maximum. *Nature* **593**, 228–232 (2021).

57. MARGO Project Members, Constraints on the magnitude and patterns of ocean cooling at the Last Glacial Maximum. *Nat. Geosci.* **2**, 127–132 (2009).

58. J. E. Tierney, J. Zhu, J. King, S. B. Malevich, G. J. Hakim, C. J. Poulsen, Glacial cooling and climate sensitivity revisited. *Nature* **584**, 569–573 (2020).

59. M. B. Osman, J. E. Tierney, J. Zhu, R. Tardif, G. J. Hakim, J. King, C. J. Poulsen, Globally resolved surface temperatures since the Last Glacial Maximum. *Nature* **599**, 239–244 (2021).

60. P. Webster, N. Streten, Late Quaternary ice age climates of tropical Australasia: Interpretations and reconstructions. *Quatern. Res.* **10**, 279–309 (1978).

61. T. R. Knutson, S. Manabe, Time-mean response over the tropical Pacific to increased $C0_2$ in a coupled ocean-atmosphere model. *J. Climate* **8**, 2181–2199 (1995).

62. J. D. Shakun, P. U. Clark, F. He, S. A. Marcott, A. C. Mix, Z. Liu, B. Otto-Bliesner, A. Schmittner, E. Bard, Global warming preceded by increasing carbon dioxide concentrations during the last deglaciation. *Nature* **484**, 49–54 (2012).

63. L. G. Thompson, E. Mosley-Thompson, K. A. Henderson, Ice-core palaeoclimate records in tropical South America since the Last Glacial Maximum. *J. Quat. Sci.* **15**, 377–394 (2000).

64. M. Meinshausen, S. Smith, K. Calvin, J. Daniel, M. Kainuma, J. Lamarque, K. Matsumoto, S. Montzka, S. Raper, K. Riahi, The paleoclimate modeling intercomparison project contribution to CMIP5. *WCRP Coupled Model Intercomp. Proj.-Phase 5-CMIP5*. **16**, 15–51 (2011).

65. M. Kageyama, P. Braconnot, S. P. Harrison, A. M. Haywood, J. H. Jungclaus, B. L. Otto-Bliesner, J.-Y. Peterschmitt, A. Abe-Ouchi, S. Albani, P. J. Bartlein, The PMIP4 contribution to CMIP6–Part 1: Overview and over-arching analysis plan. *Geosci. Model Dev.* **11**, 1033–1057 (2018).

66. E. Brady, S. Stevenson, D. Bailey, Z. Liu, D. Noone, J. Nusbaumer, B. Otto-Bliesner, C. Tabor, R. Tomas, T. Wong, J. Zhang, J. Zhu, The connected isotopic water cycle in the Community Earth System Model version 1. *J. Adv. Model. Earth Syst.* **11**, 2547–2566 (2019).

67. T. S. von Deimling, A. Ganopolski, H. Held, S. Rahmstorf, How cold was the Last Glacial Maximum? *Geophys. Res. Lett.* **33**, L14709 (2006).

68. P. B. Holden, N. Edwards, K. Oliver, T. Lenton, R. Wilkinson, A probabilistic calibration of climate sensitivity and terrestrial carbon change in GENIE-1. *Clim. Dynam.* **35**, 785–806 (2010).

69. A. Schmittner, N. M. Urban, J. D. Shakun, N. M. Mahowald, P. U. Clark, P. J. Bartlein, A. C. Mix, A. Rosell-Melé, Climate sensitivity estimated from temperature reconstructions of the Last Glacial Maximum. *Science* **334**, 1385–1388 (2011).

70. J. D. Annan, J. C. Hargreaves, A new global reconstruction of temperature changes at the Last Glacial Maximum. *Clim. Past* **9**, 367–376 (2013).

71. C. W. Snyder, Evolution of global temperature over the past two million years. *Nature* **538**, 226–228 (2016).

72. B. Bereiter, S. Shackleton, D. Baggenstos, K. Kawamura, J. Severinghaus, Mean global ocean temperatures during the last glacial transition. *Nature* **553**, 39–44 (2018).

73. T. Friedrich, A. Timmermann, Using Late Pleistocene sea surface temperature reconstructions to constrain future greenhouse warming. *Earth Planet. Sci. Lett.* **530**, 115911 (2020).

74. J. D. Annan, J. C. Hargreaves, T. Mauritsen, A new global surface temperature reconstruction for the Last Glacial Maximum. *Clim. Past* **18**, 1883–1896 (2022).

75. C. He, Z. Liu, B. L. Otto-Bliesner, E. C. Brady, C. Zhu, R. Tomas, C. Buizert, J. P. Severinghaus, Abrupt Heinrich Stadial 1 cooling missing in Greenland oxygen isotopes. *Sci. Adv.* **7**, eabh1007 (2021).

76. Z. Liu, C. He, M. Yan, C. Buizert, B. Otto-Bliesner, F. Lu, C. Zeng, Reconstruction of past Antarctic temperature using present seasonal δ18o–inversion layer temperature: Unified slope equations and applications. *J. Climate* **36**, 2933–2957 (2023).

77. D. M. Romps, Rayleigh damping in the free troposphere. *J. Atmos. Sci.* **71**, 553–565 (2014).

78. C. M. Bender, S. Orszag, S. A. Orszag, Advanced mathematical methods for scientists and engineers I: Asymptotic methods and perturbation theory (Springer Science & Business Media, 1999), 1.

79. D. Noone, Pairing measurements of the water vapor isotope ratio with humidity to deduce atmospheric moistening and dehydration in the tropical midtroposphere. *J. Climate* **25**, 4476–4494 (2012).

80. E. J. Moyer, F. W. Irion, Y. L. Yung, M. R. Gunson, ATMOS stratospheric deuterated water and implications for troposphere-stratosphere transport. *Geophys. Res. Lett.* **23**, 2385–2388 (1996).

81. G. J. Zhang, X. Wu, X. Zeng, T. Mitovski, Estimation of convective entrainment properties from a cloud-resolving model simulation during TWP-ICE. *Clim. Dynam.* **47**, 2177–2192 (2016).

82. W. C. De Rooy, P. Bechtold, K. Fröhlich, C. Hohenegger, H. Jonker, D. Mironov, A. Pier Siebesma, J. Teixeira, J.-I. Yano, Entrainment and detrainment in cumulus convection: An overview. *Q. J. Roy. Meteorol. Soc.* **139**, 1–19 (2013).

83. S. Botsyun, P. Sepulchre, Y. Donnadieu, C. Risi, A. Licht, J. K. Caves Rugenstein, Revised paleoaltimetry data show low Tibetan Plateau elevation during the Eocene. *Science* **363**, eaaq1436 (2019).

84. A. Rohrmann, M. R. Strecker, B. Bookhagen, A. Mulch, D. Sachse, H. Pingel, R. N. Alonso, T. F. Schildgen, C. Montero, Can stable isotopes ride out the storms? The role of convection for water isotopes in models, records, and paleoaltimetry studies in the central Andes. *Earth Planet. Sci. Lett.* **407**, 187–195 (2014).

85. Z. Jing, W. Yu, S. Lewis, L. G. Thompson, J. Xu, J. Zhang, B. Xu, G. Wu, Y. Ma, Y. Wang, R. Guo, Inverse altitude effect disputes the theoretical foundation of stable isotope paleoaltimetry. *Nat. Commun.* **13**, 4371 (2022).

86. P. Keil, H. Schmidt, B. Stevens, J. Bao, Variations of tropical lapse rates in climate models and their implications for upper-tropospheric warming. *J. Climate* **34**, 9747–9761 (2021).

87. O. Miyawaki, Z. Tan, T. A. Shaw, M. F. Jansen, Quantifying key mechanisms that contribute to the deviation of the tropical warming profile from a moist adiabat. *Geophys. Res. Lett.* **47** e2020GL089136 (2020).

88. P. Grootes, M. Stuiver, L. Thompson, E. Mosley-Thompson, Oxygen isotope changes in tropical ice, Quelccaya, Peru. *J. Geophys. Res. Atmos.* **94**, 1187–1194 (1989).

89. W. Stichler, U. Schotterer, K. Fröhlich, P. Ginot, C. Kull, H. Gäggeler, B. Pouyaud, Influence of sublimation on stable isotope records recovered from high-altitude glaciers in the tropical Andes. *J. Geophys. Res. Atmos.* **106**, 22613–22620 (2001).

90. K. Rozanski, L. Araguás Araguás, Spatial and temporal variability of stable isotope composition of precipitation over the South American continent. *Bull. Inst. Fr. Etudes Andin.* **24**, 379–390 (1995).

91. J. Jouzel, L. Merlivat, Deuterium and oxygen 18 in precipitation: Modeling of the isotopic effects during snow formation. *J. Geophys. Res. Atmos.* **89**, 11749–11757 (1984).

92. M. Cai, Dynamical amplification of polar warming. *Geophys. Res. Lett.* **32**, 10.1029/2005GL024481 (2005).

93. V. Masson-Delmotte, M. Kageyama, P. Braconnot, S. Charbit, G. Krinner, C. Ritz, E. Guilyardi, J. Jouzel, A. Abe-Ouchi, M. Crucifix, R. M. Gladstone, C. D. Hewitt, A. Kitoh, A. N. LeGrande, O. Marti, U. Merkel, T. Motoi, R. Ohgaito, B. Otto-Bliesner, W. R. Peltier, I. Ross, P. J. Valdes, G. Vettoretti, S. L. Weber, F. Wolk, Y. Yu, Past and future polar amplification of climate change: Climate model intercomparisons and ice-core constraints. *Clim. Dynam.* **26**, 513–529 (2006).